UNIVERSITY OF OKLAHOMA

GRADUATE COLLEGE

SUBGRID SCALE MODELING OF TURBULENCE AND CLOUD MICROPHYSICS INTERACTIONS

A THESIS

SUBMITTED TO THE GRADUATE FACULTY

in partial fulfillment of the requirements for the

Degree of

MASTER OF SCIENCE

By

CLAIRE MACKENZIE DOYLE
Norman, Oklahoma
2024

SUBGRID SCALE MODELING OF TURBULENCE AND CLOUD MICROPHYSICS INTERACTIONS

A THESIS APPROVED FOR THE
SCHOOL OF METEOROLOGY

BY THE COMMITTEE CONSISTING OF

Dr. Scott Salesky (Chair)

Dr. David Richter

Dr. Otavio Acevedo

Acknowledgments

This research would not be possible without funding from NSF award number AGS-2142982. This grant has supported me throughout my graduate research, for which I am very grateful.

I would like to thank Dr. Scott Salesky for the opportunity to work on this project. Through this work, I have gained invaluable experience and skills that I am confident I will carry with me throughout my career. I am also grateful for the support my additional committee members, Dr. David Richter and Dr. Otavio Acevedo. They have both offered their time and expertise in providing guidance and suggestions to improve my research.

I cannot thank Dr. Brian Greene enough for his mentorship throughout my time as a graduate student. For the last two years, we have met (almost) weekly and he has guided me in nearly every facet of graduate school. Whether it was coding assistance or navigating career aspirations, I could always count on him to listen and encourage me to stay true to myself.

Thank you to my office mates who were always willing to provide support, a voice of reason during tough times, or a good laugh to lighten the mood. I would also like to thank my classmates for countless hours of homework help and studying together. Thank you also to my friends and colleagues at the National Weather Center for making it a place I have called home for the past six years. I am also so grateful to my friends outside of the NWC for their constant care and cheering me on.

Finally, I would like to thank my family. They have sacrificed so much to allow me to chase my dreams of coming to OU, and have supported me every step of the way. I know they have shouldered many of the challenges I have faced, and I am so thankful for their constant patience. Words cannot express my gratitude for their love serving as a pillar of strength when I needed it most.

Table of Contents

List Of Tables

List Of Figures

Abstract

Clouds have a significant but uncertain impact on Earth's climatological and hydrological cycles. In particular, the warm rain process has considerable inconsistencies between current theories and observations. One hypothesis to explain this is the role of turbulence in broadening the droplet size distribution. The primary methods of studying these processes have been through laboratory studies, direct numerical simulations, and large eddy simulations. However, these processes are difficult to study as they occur on a broad range of scales. This makes large eddy simulations appealing as they remain computationally efficient by modeling the smallest, dissipative scales of motion. While past studies have made efforts to improve the subgrid-scale stress tensor and scalar flux vectors in large-eddy simulations, subgrid-scale terms related to cloud microphysics have received little attention. Specifically, subgrid-scale supersaturation variance is important when considering a Lagrangian microphysics approach as it arises from the Langevin equation, and both subgrid scale supersaturation and concentration covariance and subgrid scale concentration variance arise from the filtered evolution equation for droplet size distribution. It is these terms that were the focus of this study.

This study computed the true subgrid-scale variance and covariance terms from data of direct numerical simulations of Rayleigh-Bénard convection in the Michigan Technological University Pi Chamber. Five cases of varying aerosol injection rates were considered, each with a Rayleigh number of 7.9×10^6. The true subgrid-scale terms were compared to two candidate models: the gradient model and the scale-similarity model. Statistical analysis consisting of probability density functions, joint probability density functions, and correlation coefficients was used to assess model performance. Results concluded that the gradient model had relatively poor agreement with the true subgrid-scale terms with joint probability density functions that did not follow the one-to-one line which would indicate good skill, and correlation coefficients

between $\rho = 0 - 0.4$. In contrast, results from the similarity model indicated joint probability density functions that closely followed the one-to-one line, and correlation coefficients between $\rho = 0.3 - 0.9$ suggesting good agreement between the true and modeled subgrid-scale term. Altogether, the similarity model showed promise for modeling the subgrid-scale supersaturation variance, supersaturation and concentration covariance, and concentration variance. However, future investigation with higher Rayleigh numbers is warranted where larger scale separation exists between the large and small scales of turbulence.

Chapter 1

Introduction

1.1 The Importance of Clouds

The impact of clouds on Earth's climatological and hydrological systems is significant. Clouds modify the Earth's net radiative budget and can promote positive or negative climate feedbacks (Stephens and Greenwald, 1991; Stevens et al., 2005). In fact, the role of clouds in climate feedbacks remains one of the largest uncertainties when considering climate change and variability. Having a clear understanding of cloud processes can significantly improve the future predictions of climate models. While the effect of clouds influences large-scale climatology, they also have considerable impacts on smaller-scale hydrological systems.

The presence of clouds can produce precipitation which results in positive effects during a drought, or negative impacts in extreme precipitation events. The processes supporting precipitation are broadly broken down into cold rain and warm rain processes. The cold rain process refers to clouds with temperatures below freezing which results in ice clouds and mixed phase clouds. In contrast, the warm rain process is characterized by clouds with temperatures above freezing where no ice particles are present. While many knowledge gaps remain regarding ice formation and growth in cold clouds, uncertainties also remain for the processes behind warm rain–especially early in the cloud life cycle (Shaw et al., 1998). In particular, the early stages of collision-coalescence are poorly understood as large droplets ($> 30\mu m$) are required

before collision-coalescence takes place (Anderson et al., 2021; Grabowski and Wang, 2013). Various hypotheses have been developed to explain the process behind warm rain and the development of a few large droplets initiating collision-coalescence. One of these hypotheses is the likelihood of preferential growth zones due to turbulence. The following section will investigate recent research efforts behind these processes to better understand the warm rain process.

1.2 Turbulence Impacts on Cloud Microphysics

It is widely understood that clouds are turbulent in nature which can result in fluctuations in supersaturation and impact the distribution of cloud condensation nuclei in the warm rain process. In an effort to further understand the warm rain process, Beard and Ochs (1993) used observations to sample the droplet growth process. In doing so, they identified what are described as "cloud microstructures to smaller scales" which results in varying droplet sizes and concentrations. These microstructures on smaller scales were one of the initial investigations into the now, more commonly, researched topic of cloud turbulence. While cloud turbulence occurs on small scales, its significance cannot be ignored on short-term and long-term scales for meteorological and climatological events. Shaw (2003) provided support for this by stating, "If we are to understand the role of clouds in human affairs and the global environment, we are obliged to increase our understanding of processes occurring on seemingly unrelated scales, such as cloud-droplet activation and the subsequent temporal and spatial evolution of cloud-particle size distributions." As stated previously, there are many components of small-scale turbulence that can result in significant impacts on cloud physics processes. In a recent review article, Grabowski and Wang (2013) states two significant results from cloud turbulence studies: 1) "...small-scale turbulence alone does not produce

a significant broadening of the cloud-droplet spectrum," and, 2) "...small-scale turbulence in cumulus clouds makes a significant contribution to the collision-coalescence of droplets..." Vaillancourt and Yau (2000) supported that proper conditions could improve collision efficiency within the clouds and could be a significant contributor to precipitation development. However, a deeper understanding of the way turbulence is characterized in clouds is necessary to fully understand the broader implications.

Quantifying the "small scales" that are referred to when discussing cloud turbulence is important. Generally speaking, these small scales are on the order of micrometers to millimeters. Shaw (2003) states, "These scales are fundamental to the microscale physics of droplet growth, which determines spatial and temporal variations in the droplet size distribution." In addition, Shaw (2003) characterizes these small scales "by large Reynolds numbers, small energy dissipation rates, moderate rms velocities, and a large inertial subrange spanning several orders of magnitude." Since turbulence takes place on such fine scales, airborne observations of cloud microphysics are more challenging to use when investigating turbulent structures (Shaw, 2003). In an effort to understand some of these small-scale, turbulent processes, several other methods of investigation have been used and will be the focus of this introduction: laboratory studies, direct numerical simulations, and the utility of large eddy simulations.

1.3 Recent Research Endeavors

As noted previously, accurate observations of cloud turbulence are limited in the real atmosphere. This is due to complexities in data collection including the location of warm clouds and limitations in observational platforms related to the small scales of interest. To aid in further understanding, other methods can provide more data volume and pointed investigations when studying cloud turbulence.

1.3.1 Pi Chamber

One method for cloud turbulence research is laboratory experiments. A prominent experimental facility for studying cloud-aerosol-turbulence interactions is the Pi Chamber at Michigan Technological University. The Pi Chamber is a laboratory chamber with a volume of 3.14 m^3 used to study cloud microphysics within steady-state conditions (Chang et al., 2016). The chamber has a warm plate on the floor and a cool plate on the ceiling which results in buoyancy-driven turbulent motions and Rayleigh-Bénard convection (Anderson et al., 2021; Chang et al., 2016). Rayleigh-Bénard convection is characterized by a large-scale circulation within smaller turbulent fluctuations (Anderson et al., 2021). Further, this large-scale circulation was found to oscillate from the mean circulation, but more detail on this can be found in Anderson et al. (2021). Since the steady-state conditions can be observed for hours to days, this can provide extremely useful data on fluctuating turbulent structures for long periods of time. The primary objectives for the development of the Pi Chamber were to gain better understanding of the distributions of temperature, water vapor, droplet size, and other relevant thermodynamic and cloud microphysical characteristics in turbulent environments.

Recent studies have investigated these processes and have found evidence that turbulence has an influential role in cloud microphysics. Prabhakaran et al. (2020) found that there are two regimes with which droplets become activated. The first is a mean-dominated regime and the second is a fluctuation-dominated regime. The mean-dominated regime is characterized by mean supersaturations within the chamber. However, the fluctuation-dominated regime is classified by mean subsaturated conditions within the chamber, but greater turbulent motions. The study was conducted by injecting aerosol particles at a steady rate into the chamber to support cloud activation. This was conducted at varying mean saturation ratios controlled by

the temperature profiles within the chamber. Throughout the process of droplet activation, the droplet size distribution was observed with an optical particle counter. Since this study observed activated cloud particles in both mean supersaturated conditions as well as unsaturated conditions, the results support the idea that turbulence can provide preferential growth zones where there are above-average saturation ratios while also promoting greater droplet size distributions than the environmental mean (Prabhakaran et al., 2020).

Similar to Prabhakaran et al. (2020), Shawon et al. (2021) also injected aerosol particles into the chamber. In contrast to Prabhakaran et al. (2020), measurements of temperature and water vapor were evaluated with thermistors and hygrometers rather than relying on the mean saturation ratio conditions. With data on the temperature and water vapor, the saturation ratio could be calculated to determine fluctuations within the chamber which would indicate possible preferential droplet growth zones. Some of this study's key findings suggest that turbulence can impact the relationship between a particle's size and chemical makeup due to saturation ratio fluctuations in a turbulent flow. In addition, turbulence can increase the number of activated cloud droplets due to temperature fluctuations likely resulting in preferential growth zones (Shawon et al., 2021). These findings support Prabhakaran et al. (2020) where the fluctuation-dominated regime resulted in cloud droplet activation even in unsaturated conditions. While these were not necessarily unsaturated conditions, this still suggests preferential growth areas where droplets have greater than average droplet size distributions correlated to above-average saturation ratios.

Finally, Anderson et al. (2021) studied the spatial distribution of saturation ratio throughout the chamber. Similar methods to Shawon et al. (2021) were used with the thermistors and hygrometers. Since these measurements could only be taken at

specific points, this study wanted to investigate how path-averaged and point measurements of supersaturation differed. To evaluate this, the collected data was applied to a large eddy simulation to determine the path-averaged values of temperature and water vapor. With these, the path-averaged saturation ratio could be computed. The results concluded that there were significant fluctuations in each of these variables. In addition, the temperature and mixing ratio were positively skewed near the updrafts and negatively skewed near the downdrafts. In contrast, the saturation ratio was always negatively skewed, but more negatively skewed near the downdraft. Anderson et al. (2021) comments on the importance of these fluctuations by stating, ". . . spatial variations of the mean in the chamber may affect, for example, where droplets preferentially activate or evaporate." This is further evidence supporting the ideas already proposed and observed by Prabhakaran et al. (2020) and Shawon et al. (2021). However, this article does propose an important issue that, while laboratory experiments are extremely valuable, they do lack the ability to fully understand particle history. Further, this study uses one of the more prominent methods of investigation in the cloud turbulence community- numerical simulations. The numerical simulation approach will be further discussed in the following sections.

1.3.2 Direct Numerical Simulations

Direct numerical simulations (DNS) are a powerful tool in turbulence research as they can fully resolve the entire spectrum of turbulence, including the smallest dissipative scales of motion. Even early studies investigating turbulence impacts on cloud microphysics provided important discoveries. For example, the first study to simulate the condensational growth process within a turbulent flow was Vaillancourt et al. (2002). Their results concluded that there were areas of preferential concentration within regions of low vorticity. However, the results also concluded that there were narrower

droplet distributions in a turbulent flow than in a flow without turbulence (Vaillancourt et al., 2002; Shaw, 2003). This study had several limitations including Reynolds numbers lower than cumulus clouds and the model not accounting for droplet-diffusive interactions (Vaillancourt et al., 2002). These limitations may have greatly impacted the authors' results. With improvements in technology and increases in computing power, more recent studies have been conducted and are more aligned with the findings outlined previously.

Kumar et al. (2018) investigated the impacts of turbulent mixing and entrainment on droplet size distributions. This study was conducted by simulating two planes– one with a clear air interface and one with supersaturated air and varying domain sizes. Lagrangian droplet particles were simulated to provide information on droplet position and growth. In addition, information on liquid water content and supersaturation could be determined. Further information on the model configuration can be found in Kumar et al. (2013, 2014). The results of this study concluded that droplet distribution is strongly dependent on the spatial scale of a turbulent flow. This indicates that the scale with which mixing takes place will have a significant impact on the degree to which particles become activated (Kumar et al., 2018). These results supported those of previous works such as Grabowski and Wang (2013) which summarized that entrainment is a multi-scale process that has significant impacts on the growth of cloud droplets. However, Grabowski and Wang (2013) also summarized that small-scale turbulence alone is not the sole contributor to a broader droplet size distribution, but can contribute to large-eddy hopping. Large-eddy hopping would allow particles to be transported from smaller eddies to larger eddies, greatly impacting their droplet growth history (Grabowski and Wang, 2013).

Similar work was conducted by Thomas et al. (2020) where DNS was used to simulate the impact of homogeneous isotropic turbulence on cloud microphysics and

investigate methods to improve the simulation of these processes. The general model configuration was based on the simulations investigated in Lanotte et al. (2009). In addition to a real DNS, a "scaled-up DNS" model was developed and used for these studies. The scaled-up DNS is able to increase the domain and use super-droplets to represent a group of droplets rather than simulating individual droplets. Finally, a stochastic model similar to Grabowski and Abade (2017) was used to model supersaturation fluctuations and serve as a method for comparison of real and scaled-up DNS models. The results of this study suggest that both the droplet size distribution and supersaturation fluctuations increased with increasing domain size. In addition, Thomas et al. (2020) states, "One can argue that scale-dependent supersaturation fluctuations can induce significant droplet concentration heterogeneities at the cloud base that arguably affect droplet growth aloft." Not only does this support previous DNS studies, but it also supports findings from the Pi Chamber that suggest alterations in droplet growth history due to turbulent fluctuations.

Further investigations related to the Pi Chamber was a study conducted by MacMillan et al. (2022) which used a DNS to simulate the processes within the chamber. To simulate this, the model had solid walls at both the top and bottom of the simulation. In addition, there were temperature and relative humidity fluxes applied to the top and bottom of the simulation to replicate the warm and cool plates within the chamber. The key difference between this model and the Pi Chamber were that the simulated Rayleigh numbers (7.9×10^6) were lower than the laboratory experimental values ($Ra \sim 10^9$). In addition, there were no sidewalls within the simulation, but a periodic domain in the horizontal direction (Thomas et al., 2019; MacMillan et al., 2022). The sidewalls in the Pi Chamber result in condensation which acts as a humidity sink and limits the maximum relative humidity within the chamber. To account for this in the DNS, a sink term was applied in the model to ensure consistency. Similar to

other previous studies, this model also used Lagrangian superdroplets. More detailed information on the model configuration can be found in Richter et al. (2021). The results from this study suggest that features such as aerosol activation rates in the DNS perform well compared to the results from the Pi Chamber. However, there were some important findings in contrast to those found in the chamber. When the Lagrangian particles were investigated, they were found to have significant differences in supersaturation fluctuations than the results measured from an Eulerian perspective. This study observed non-Gaussian distributions with heavy tails within the Lagrangian distributions as compared to the Gaussian-distributed supersaturation fluctuations observed in the Pi Chamber. In addition, droplets underwent multiple periods of activation and deactivation. As noted by MacMillan et al. (2022), these results may have significant impacts on how accurately models predict cloud microphysical processes. Additional details on the role of DNS in future microphysical studies will be explored in this review.

1.3.3 Large Eddy Simulations

Similar to DNS, large eddy simulations (LES) are also commonly used to study turbulence. The difference between DNS and LES is that DNS can fully resolve the smallest scales of motion while LES must model the smallest scales and fully resolve the largest eddies in the flow. Modeling the effects of the small scales (below the model's grid spacing) is done with subgrid-scale models. Methods for representing microphysical processes in LES include bulk, bin, and Lagrangian microphysics schemes. Bulk schemes make predictions about particle characteristics that are related to the moments of a particle size distribution (Hu and Igel, 2023). As such, the shape of the droplet size distribution is assumed a priori. Since particle characteristics are predicted rather than explicitly solved, bulk schemes are the least computationally expensive (Khain et al.,

2015; Shima et al., 2009). However, this decreased computational expense results in greater inaccuracies (Khain et al., 2015; Shima et al., 2009). Due to these limitations in accuracy, bulk schemes are primarily used for operational models leaving bin and Lagrangian schemes for research purposes (Morrison et al., 2020).

Bin schemes explicitly solve the evolution equations for particle characteristics within certain size or mass ranges (Hu and Igel, 2023; Grabowski, 2020; Morrison et al., 2020). While this method produces more accurate results, they are more computationally expensive (Hu and Igel, 2023; Morrison et al., 2020; Khain et al., 2015; Shima et al., 2009). However, inaccuracies in the broadening of the droplet size distributions arise when vertical advection is incorporated (Morrison et al., 2018). In addition, they become more computationally expensive with increasing variables to predict (Morrison et al., 2020). To balance computational expense and accuracy, the Lagrangian method was developed (Shima et al., 2009). This method tracks an ensemble of particles with the same properties (i.e., position, velocity, radius, etc.), known as superdroplets, as they evolve in a fluid flow (Grabowski, 2020). Despite being limited by the number of superdroplets that can be tracked in a given model, this method is less computationally expensive while maintaining accuracy making it a useful subgrid-scale tool (Grabowski, 2020). With a variety of subgrid-scale models, LES has been a method used to investigate cloud microphysics and turbulence for decades (Thomas et al., 2019). Over the years, this science has greatly improved the understanding of the intersection between these two research areas. However, since the effects of the smallest scales of motion must be modeled in LES, comparisons with field research studies, laboratory studies, and other models are important to ensure an accurate representation of the small scales. This section will explore some studies that have investigated these topics.

An important intercomparison study between LES and observations in marine stratocumulus clouds was conducted by Stevens et al. (2005). This study used observations

from the second Dynamics and Chemistry of Marine Stratocumulus (DYCOMS-II) field campaign and 10 different LES models. Each of the models were initialized from the observed conditions from the DYCOMS-II campaign. While the grid spacing, time series, and thermodynamic calculations were standardized, models were allowed to have different numerical algorithms and subgrid-scale schemes. Further detail about each of the models and the cases used for comparison can be found in Stevens et al. (2005). The results from this study conclude that altering vertical grid spacing or subgrid models to reduce mixing at the cloud top compares well to the observations. However, the base configuration overestimates mixing at the top of clouds which then underestimates turbulence and liquid water path. Finally, it was identified that there is greater sensitivity to the details of observed data when representing mixing at cloud tops (Stevens et al., 2005). This study is closely related to the results of Grabowski and Wang (2013) which outlined the complications of entrainment as a multi-scale process relating to droplet growth. It is further summarized by Devenish et al. (2012) where it is stated that modeled subgrid scale eddies may be contributing to the entrainment rate in addition to large-scale eddies resolved by LES. This highlights an important complication of LES modeling— the challenge of implementing accurate subgrid-scale modeling schemes.

In an effort to better understand and quantify droplet size distributions from various models, Morrison et al. (2018) investigated three different modeling frameworks in LES that use bin microphysics to identify the most realistic method. The frameworks compared in this study were parcel, one-dimensional, and three-dimensional models. This study used Smagorinsky methods for subgrid-scale mixing and follows various previous studies for model configuration, but these details can be found in Morrison et al. (2018). The key findings from this study suggest that droplet size distribution broadening is primarily driven by numerical diffusion resulting from vertical advection in the resolved

flow when bin microphysics are used (Morrison et al., 2018). This was determined by a model where Eulerian transport was neglected, but droplet size distributions were comparable to Lagrangian processes previously understood and accepted. However, it is important to note that the reasoning behind this broadening droplet size distribution may not be physical. In addition, Morrison et al. (2018) suggested that droplet size distribution variability and droplet size distribution broadening from mixing are underrepresented in LES models. Further, Morrison et al. (2018) stated, "It is reasonable to think that unphysical broadening from vertical numerical diffusion compensates for underrepresenting or neglecting these physical broadening mechanisms." As such, it is also mentioned that new methods should be developed to accurately model these processes which will be further explored in the future works section (Morrison et al., 2018).

Similar to the work of MacMillan et al. (2022), Thomas et al. (2019) simulates the Pi Chamber with a numerical model but uses LES rather than DNS. The LES in this study uses turbulent kinetic energy (TKE) to model the subgrid scales (SGS) where the smallest scales of motion are located. This study also has solid walls for the top, bottom, and sidewalls. In addition, it uses Monin-Obukhov similarity theory to simulate fluxes at each of these walls. Finally, it uses spectral bin microphysics which serves to simulate the aerosol-cloud interactions. Additional information on the LES configuration can be found in Thomas et al. (2019). When this study was conducted, the results concluded that this model portrayed microphysical processes that were consistent with the results found in the Pi Chamber. This included Gaussian distributed supersaturation, droplet size distributions increasing with decreasing droplet number density, and the process of condensational growth being the dominant growth process (Thomas et al., 2019). However, the finding of Gaussian distributed supersaturation is not consistent with the more recent findings from MacMillan et al. (2022). This may

suggest that the LES is not adequately resolving the small scales while the Pi Chamber does not gain enough information from an Eulerian perspective. More information on how the LES subgrid scales can be improved will be discussed in the next section.

1.4 Current Knowledge Gaps

One of the outstanding research efforts the cloud physics community pursues is fully understanding the warm rain process. Turbulence impacts on cloud microphysics have been one of the hypotheses for furthering the current knowledge. Turbulence may have a significant effect as it can provide preferential growth regions as a result of supersaturation fluctuations. The primary methods of research on this topic have been through laboratory experiments and numerical modeling since field studies are difficult to investigate small-scale cloud microphysical changes with time. While recent studies have supported this and have contributed significantly to current understanding, there is a lot to investigate to ensure accurate interpretations and representations of these processes. While there are many ways laboratory studies could be improved, such as the development of larger cloud chambers with larger residence times required for collision-coalescence, this analysis will primarily focus on improving numerical modeling.

Many of the studies outlined in this introduction have noted the limitations of numerical models and where future works efforts should be focused. DNS is a powerful tool when modeling cloud turbulence as it can fully resolve the smallest scales of motion. However, its utility within larger domains is limited as it becomes too computationally expensive. As a result, LES models are often used as it is less computationally expensive. LES stays computationally efficient as it fully resolves large-scale motions but models the smaller scales. This then results in challenges as the smaller scales must be properly modeled in order to remain physically accurate.

Many previous studies have focused on improving models for SGS stress tensor and scalar flux vectors (Liu et al., 1994; Porté-Agel et al., 2001; Sullivan et al., 2003; Higgins et al., 2007; Chumakov, 2008). While these have improved LES modeling, few studies have investigated SGS models for interactions between turbulence and cloud microphysics. In particular, uncertainties arise in bin microphysics with the evolution equation for the droplet size distribution where droplets are binned by radius or mass. This equation is given as:

$$\frac{\partial f(r)}{\partial t} + \nabla \cdot \left[\mathbf{v_p} f(r)\right] + \frac{\partial}{\partial r}\left[\frac{\gamma}{r} s f(r)\right] = J(r) + \frac{1}{2}\int_0^r \frac{r^2}{r''^2}\Gamma_{12}\left[r'', r'\right] f(r'') f(r') dr' - \int_0^\infty \Gamma_{12}(r, r') f(r) f(r') dr' \tag{1.1}$$

where r is droplet radius, $\mathbf{v_p}$ is droplet velocity, s is supersaturation, J is rate of nucleation, Γ_{12} is the collision kernel, and γ is a function of temperature and pressure (Yau and Rogers, 1996). The terms on the left-hand side (from left to right) are the local change of droplet size distribution, advection, and condensation/evaporation. On the right-hand side, the terms are (from left to right) nucleation, production of droplets of radius r by collision-coalescence, and loss of droplets of radius r by collision coalescence. These terms maintain contributions from all scales of motion. If equation 1.1 is low pass filtered, consistent with typical LES methods (Pope, 2000), the resolved scale droplet size distribution evolution equation is as follows:

$$\begin{aligned}\frac{\partial \widetilde{f}(r)}{\partial t} + \nabla \cdot \left[\widetilde{\mathbf{v_p}} \widetilde{f}(r)\right] + \frac{\partial}{\partial r}\left[\frac{\gamma}{r}\widetilde{s}\widetilde{f}(r)\right] &= \widetilde{J}(r) + \frac{1}{2}\int_0^r \frac{r^2}{r''^2}\Gamma_{12}(r'', r')\widetilde{f}(r'')\widetilde{f}(r') dr' \\ &- \int_0^\infty \Gamma_{12}(r, r')\widetilde{f}(r)\widetilde{f}(r') dr' - \frac{1}{\rho_a}\nabla \cdot \pi_{v_p, f(r)} - \frac{\partial}{\partial r}\left[\frac{\gamma}{r}\chi_{s, f(r)}\right] \\ &+ \frac{1}{2}\int_0^r \frac{r^2}{r''^2}\Gamma_{12}(r'', r')\chi_{f(r''), f(r')} dr' - \int_0^\infty \Gamma_{12}(r, r')\chi_{f(r), f(r')} dr'.\end{aligned} \tag{1.2}$$

From this, terms emerge that represent the SGS supersaturation and concentration covariance ($\chi_{s,f(r)} = \widetilde{sf(r)} - \widetilde{s}\widetilde{f}(r)$) of particle radius, r, and the SGS concentration covariance ($\chi_{f(r),f(r')} = \widetilde{f(r)f(r')} - \widetilde{f}(r)\widetilde{f}(r')$) of particles with radius r and r'. The terms on the left-hand side are (from left to right) the local change of the resolved scale droplet size distribution, resolved scale advection, and resolved scale condensation/evaporation. On the right-hand side, the terms are (from left to right) the resolved scale nucleation, production of droplets of radius r by the resolved-scale collision coalescence, loss of droplets of radius r by the resolved scale collision coalescence, transport of droplets due to the SGS covariance between the droplet size distribution and particle velocity, SGS condensation/evaporation, production of droplets of radius r by SGS collision coalescence, and loss of droplets of radius r by SGS collision coalescence. Current LES models solve the resolved scale terms and neglect the terms for the SGS condensation/evaporation, production of droplets of radius r by SGS collision coalescence, and loss of droplets of radius r by SGS collision coalescence. In addition, supersaturation fluctuations are important when considering Lagrangian microphysics as they determine the condensational growth of cloud droplets. Typically, these are modeled with the Langevin equation which includes the supersaturation variance within the stochastic term (Pope, 2000; Grabowski and Abade, 2017). The supersaturation variance can be broken down into resolved and subgrid-scale components ($\langle S'^2 \rangle = \langle \widetilde{S}'^2 \rangle + \langle \tau_{SS} \rangle$) where τ_{SS} is the SGS supersaturation variance which must be modeled.

At this time, few studies have investigated these terms to develop SGS models. Some recent studies have created SGS models for the supersaturation variance with a linear eddy model, while Lagrangian-based studies have used stochastic methods (Grabowski and Abade, 2017; Hoffmann and Feingold, 2019). However, Salesky et al. (2024) evaluated the SGS supersaturation variance of data collected in the Pi Chamber with a priori tests. This approach will be investigated in this thesis and applied

to SGS terms including supersaturation variance, supersaturation and concentration covariance, and concentration variance.

Chapter 2

Data and Methods

2.1 DNS Code

This study conducted a series of simulations with direct numerical simulations (DNS) of Rayleigh-Bénard convection consistent with the Pi Chamber from Michigan Technological University. These simulations were completed using the Cheyenne cluster at the National Center for Atmospheric Research (NCAR) as part of a small computing allocation. This study closely follows the methods outlined in MacMillan et al. (2022) which used the NCAR Turbulence with Lagrangian Particles (NTLP) model described in Richter et al. (2021). However, details of the relevant methods are outlined below.

2.1.1 Eulerian Flow Fields

This model explicitly solves the Navier-Stokes equation for momentum in addition to the scalar advection diffusion equations for temperature and humidity which provide an Eulerian flow field. These equations were subject to the Boussinesq approximation and are given as the following:

$$\nabla \cdot \mathbf{u} = 0, \tag{2.1}$$

$$\frac{\partial \mathbf{u}}{\partial t} + \mathbf{u} \cdot \nabla \mathbf{u} = -\nabla \pi + \widehat{\mathbf{k}} \frac{g}{T_0} T_v' + \nu \nabla^2 \mathbf{u} + \mathbf{S}_m, \tag{2.2}$$

$$\frac{\partial T}{\partial t} + \mathbf{u} \cdot \nabla T = \alpha \nabla^2 T + S_T, \tag{2.3}$$

$$\frac{\partial q_v}{\partial t} + \mathbf{u} \cdot \nabla q_v = \Gamma \nabla^2 q_v + S_v, \tag{2.4}$$

where $\mathbf{u}$ is the velocity vector of the fluid, T is the temperature, and q_v is the water vapor mixing ratio. Further, π is a pressure variable that enforces incompressibility and $\widehat{\mathbf{k}}$ is the vertical unit vector for gravitational acceleration, g. The reference temperature, T_0 equals 300 K, and T_v' is the virtual temperature perturbation. Finally, ν, α, and Γ are the diffusivities for momentum, temperature, and water vapor, while $\mathbf{S}_m$, S_T, and S_v are source terms for momentum, temperature, and vapor as a result of the droplets. Further details on the expanded expressions for the source terms can be found in Richter et al. (2021). Each of these equations is solved with second-order finite differencing in the vertical direction while horizontal derivatives were calculated using the psuedospectral approach. Details on the boundary conditions applied to this simulation will be discussed in a later section.

2.1.2 Lagrangian Particles

Similar to the Pi Chamber, aerosols were injected in the simulations, where they were represented using a superdroplet scheme (Shima et al., 2009). The superdroplet method is characterized by a set of droplets each of which represent an ensemble of droplets with the same characteristics. Different injection rates were simulated by changing the multiplicity, or the number of particles one superdroplet represents. With this scheme, Lagrangian particle information including particle location ($\mathbf{x}_p$), velocity ($\mathbf{v}_p$), temperature (T_p), and radius (r) was maintained. The evolution equations for these processes were as follows:

$$\frac{d\mathbf{x}_p}{dt} = \mathbf{v}_p, \tag{2.5}$$

$$\frac{d\mathbf{v}_p}{dt} = \frac{1}{\tau_p}(\mathbf{u} - \mathbf{v}_p), \tag{2.6}$$

$$\frac{dT_p}{dt} = \frac{1}{\tau_T}(T_f - T_p) + \frac{\gamma_T}{r}\frac{dr}{dt}, \tag{2.7}$$

$$\frac{dr}{dt} = \gamma_q \frac{r}{\tau_p}(q_v - q_\star), \tag{2.8}$$

where the particle information is fully two-way coupled to the background flow through the temperature of the fluid (T_f), the velocity of the fluid ($\mathbf{u}$), and the water vapor mixing ratio of the fluid (q_v). Further, $q_\star$ is the water vapor mixing ratio at the particle surface as derived from Köhler theory. Finally, τ_p and τ_T represent inertial and thermal time constants while γ_T and γ_q are coefficients that account for processes such as specific heat, density, and heat transfer. In addition, these equations were integrated with an implicit, backward Euler scheme. Further information on the injection rates assessed will be discussed in the following section.

2.2 DNS Cases

To remain similar to the Pi Chamber, the domain of the DNS was 2m x 2m x 1m with grid spacing of 128^3. The simulations were run with a third-order Runge-Kutta scheme that had a constant time step (Δt) of 0.05 s for 5000 s. Further, the relative humidity at the bottom and top boundaries was set to 100% to ensure a saturated

environment for droplet activation. Also consistent with the Pi Chamber was the initiation of Rayleigh-Bénard convection by warm and cool boundary conditions simulating the warm and cool plates present in the chamber. These boundary conditions are consistent with those outlined in MacMillan et al. (2022), and were prescribed to be 299K at the bottom boundary and 280 K at the top boundary. Further, the aerosol injection rate was varied by changing the multiplicity of the superdroplets (i.e., how many particles one superdroplet represents). For this study, five injection rates were simulated: $1\text{cm}^{-3}\,\text{min}^{-1}$, $3\text{cm}^{-3}\,\text{min}^{-1}$, $10\text{cm}^{-3}\,\text{min}^{-1}$, $30\text{cm}^{-3}\,\text{min}^{-1}$, and $100\text{cm}^{-3}\,\text{min}^{-1}$. All simulation case settings are displayed in Table 2.1.

Variable	**Value**
Domain $[L_x \times L_y \times L_z]$	$2\,\text{m} \times 2\,\text{m} \times 1\,\text{m}$
Grid points $[N_x, N_y, N_z]$	128, 128, 128
Timestep $[\Delta t]$	0.05 s
Temperature $[T_{bottom}, T_{top}]$	299, 280 K
Relative humidity $[RH_{bottom}, RH_{top}]$	100, 100%
Rayleigh number [Ra]	7.9×10^9
Aerosol injection rate $[\dot{n}]$	1, 3, 10, 30, 100 $\text{cm}^{-3}\,\text{min}^{-1}$

Table 2.1: Simulations setting for each of the five cases where aerosol injection rate was varied.

While the simulation remains similar to the conditions of the Pi Chamber, one difference lies in the Rayleigh numbers. Rayleigh numbers for this flow can be defined as:

$$Ra = \frac{g\,\Delta T\,L_z^3}{T_0\,\nu\,\alpha} \tag{2.9}$$

where g is the gravity of the fluid (set to a constant, $g = 0.043\,\text{m}\,\text{s}^{-2}$), ΔT is the difference between the top and bottom boundary conditions for temperature, L_z is the vertical domain, T_0 is the reference temperature, 300 K, and ν and α are the diffusivities

for momentum and temperature. With these given parameters, the simulation results in a Rayleigh number of approximately 7.9×10^6. While this is lower than the Pi Chamber ($Ra \sim 10^9$), the DNS is limited by computational expense. However, future work with this study will increase the Rayleigh numbers simulated.

As droplets are able to activate into cloud condensation nuclei within the simulation, maintaining information on the size of the activated droplets is significant. This allows for a comparison between the particle size and background flow characteristics. In particular, relationships between particle size and fluid supersaturation are of interest. Supersaturation, s, is defined as:

$$s = \frac{e}{e_s(\theta)} - 1 \tag{2.10}$$

where e is the vapor pressure and $e_s(\theta)$ is the saturation vapor pressure dependent on temperature. However, supersaturation in the cases within this study was much higher than that of the Pi Chamber and may influence the relationship between particle size and supersaturation. Future studies will apply a humidity correction available in the simulation parameters. Finally, while the model is capable of resolving the collision coalescence process, this was not implemented in this study. The collision coalescence process may be beneficial for future studies of cloud turbulence processes. Any further information on the simulation configuration can be found in MacMillan et al. (2022) or Richter et al. (2021).

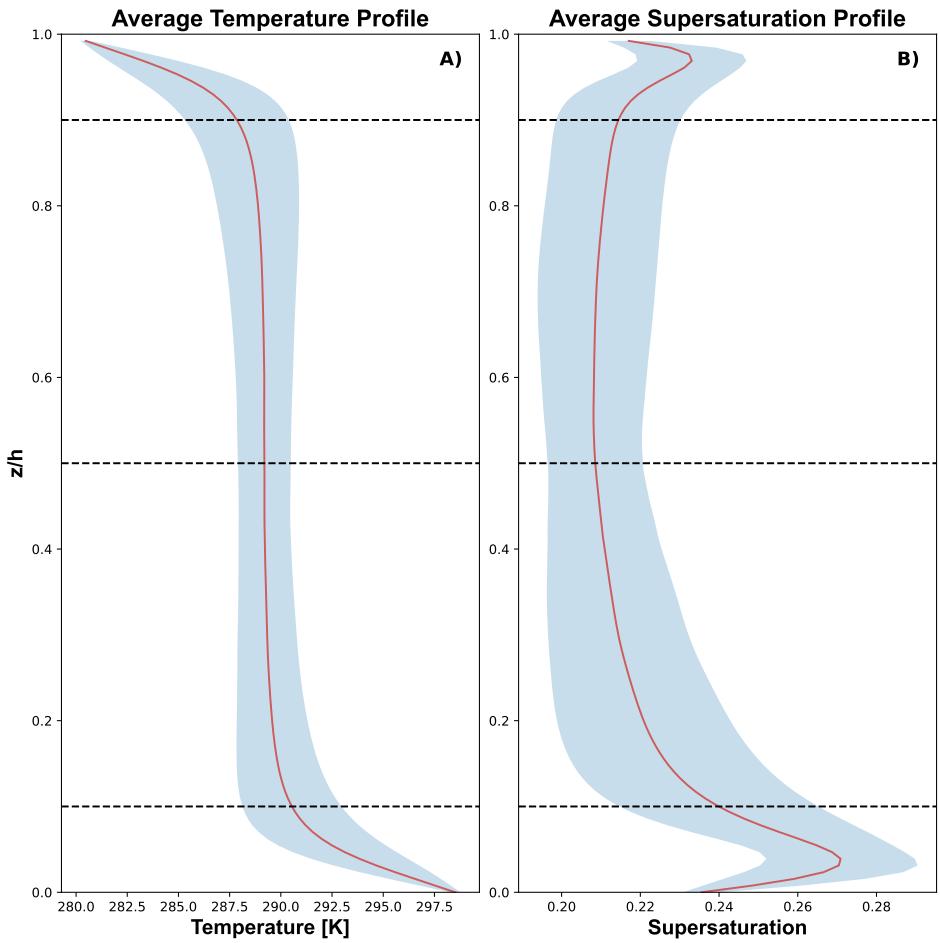

Figure 2.1: Horizontal and temporal average of temperature (a) and supersaturation (b) profiles with height where blue shading represents the standard deviation. In addition, black dashed lines represent heights 0.1m, 0.5m, and 0.9m.

2.3 Analysis Techniques

2.3.1 Data Processing

As noted previously, the DNS was configured to simulate cloudy, turbulent Rayleigh-Bénard convection consistent with the Pi Chamber. Due to the heating applied to the bottom and top boundaries inducing Rayleigh-Bénard convection, boundary layer features were observed near the top and bottom boundaries. However, the fluid became well mixed in the center of the domain. These features are visualized when considering

the vertical profiles of temperature and supersaturation in Figure 2.1. The boundary layer features are significant as the flow and particles may behave differently within this regime. As such, this analysis identifies three heights for comparison: 0.1 m, 0.5 m, and 0.9 m as denoted in Figure 2.1. The heights selected sample near the top and bottom boundary layers in addition to the well-mixed layer. However, further considerations for the variables of interest must also be made.

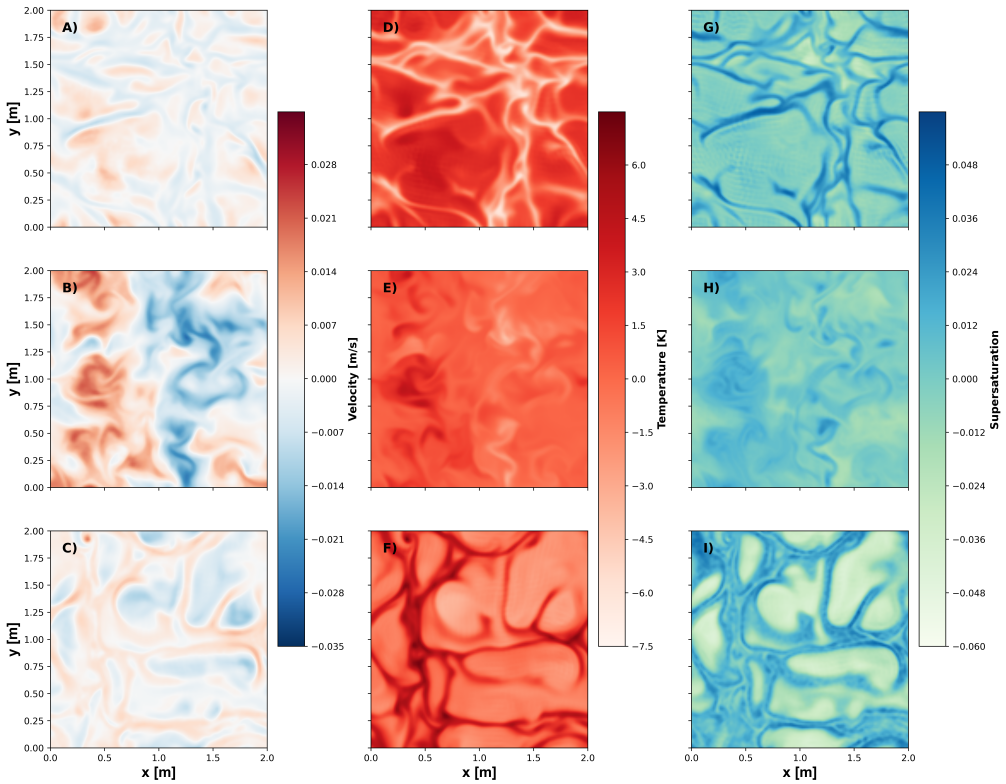

Figure 2.2: Contours of fluctuations for vertical velocity (a-c), temperature (d-f), and supersaturation(G-I) at heights 0.1m (c, f, and i), 0.5m (b, e, and h), and 0.9m (a, d, and g) for an arbitrary time.

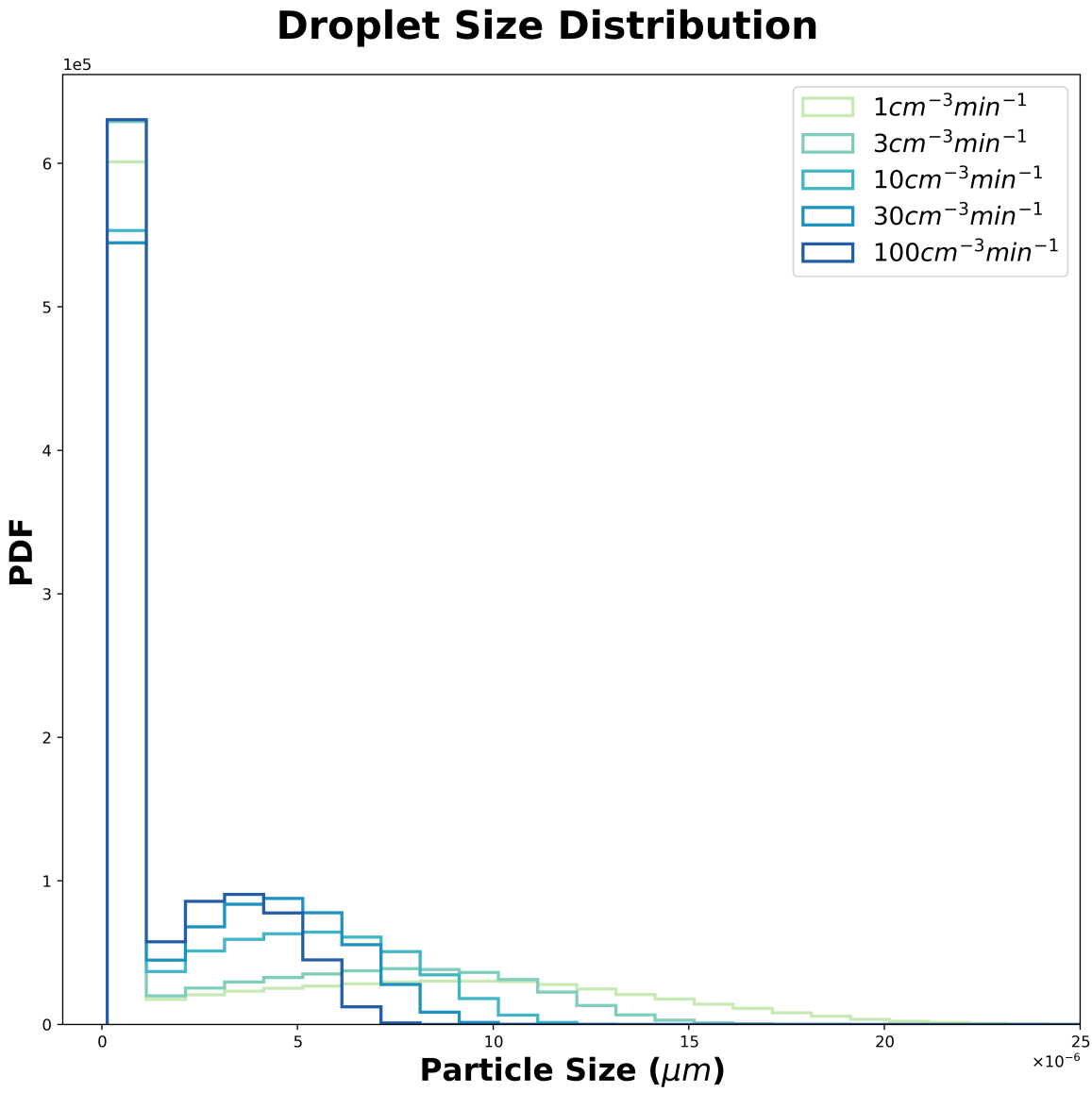

Figure 2.3: Droplet size distributions for each case of varying injection rates: $\dot{n}$= 1, 3, 10, 30, and 100cm^{-3} min^{-1}.

In addition to the large-scale circulation characteristic of Rayleigh-Bénard convection, small-scale fluctuations are pertinent. These fluctuations are defined through Reynolds decomposition which defines the fluctuation as how much the true value departs from the mean quantity ($a' = a - \langle a \rangle$). These fluctuations can be observed by the horizontal contours of vertical velocity, temperature, and supersaturation at the

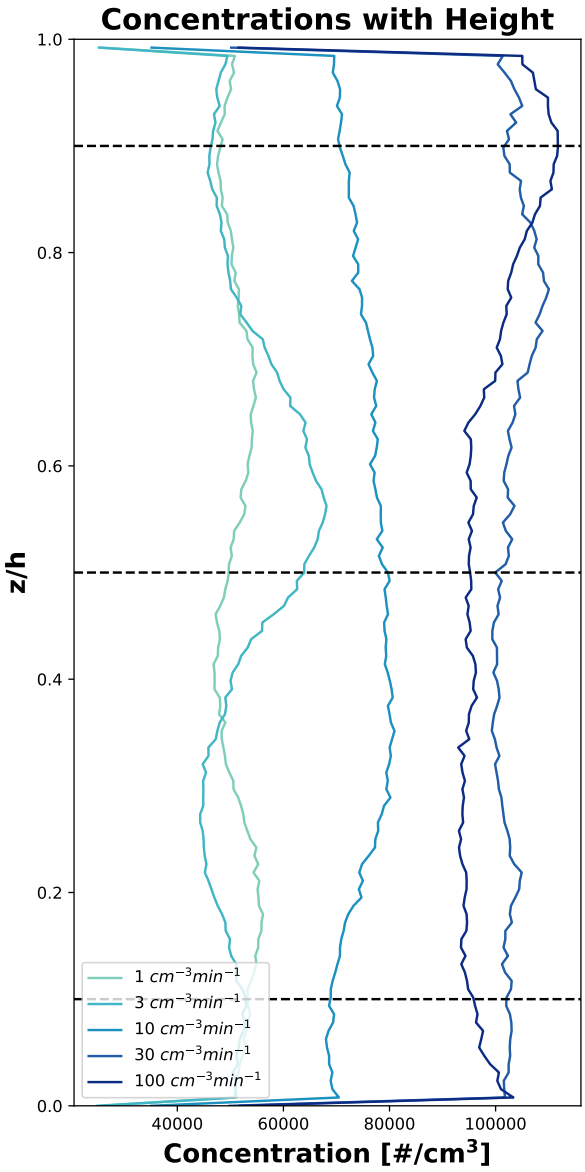

Figure 2.4: Horizontal and temporal average of concentration profiles with height for each injection rate. In addition, black dashed lines represent heights 0.1m, 0.5m, and 0.9m.

previously selected heights (Fig. 2.2). The large-scale updraft is evident on the left side of the domain with a broad downdraft on the right side of the domain (Fig. 2.2 b). However, the fluctuations can be visualized where the large-scale circulation is still present. It is these fluctuations, particularly when considering supersaturation, that are of interest in this study.

When considering the Lagrangian particles, each particle was assigned to the nearest grid cell within the domain. Further, the number of particles in each grid cell was counted and binned according to size. Three particle size bins were used: $< 1\mu m$, 1–5 μm, and $> 5\mu m$. These bins were determined from the droplet size distribution of all particles for each case (Fig. 2.3). With the given particle bins, the concentration of particles at each grid point was calculated. The horizontally averaged vertical profile of these concentrations is displayed in Figure 2.4. Since the DNS explicitly resolves the particle activation process, particles corresponding to unactivated aerosols ($< 1\mu$m) were neglected in this study. Therefore, only concentrations of activated cloud droplets ($> 1\mu$m) were used for analysis. As expected, the number of particles increased with increasing injection rate. However, the largest injection rate case (100 $\mathrm{cm}^{-3}\,\mathrm{min}^{-1}$) had lower concentrations than the second largest injection rate (30 $\mathrm{cm}^{-3}\,\mathrm{min}^{-1}$). It is believed that this is due to a lack of statistical convergence, or it could be due to large droplets falling out of the domain. Regardless, further investigation into this observation should be evaluated in future work.

2.3.2 Subgrid Scale Terms

With the Eulerian flow fields and Lagrangian particle information, several subgrid-scale quantities can be investigated including supersaturation variance (τ_{SS}), supersaturation and concentration covariance (τ_{SC}), and concentration variance (τ_{CC}). Each of these terms is defined as:

$$\tau_{SS} = \widetilde{SS} - \widetilde{S}\widetilde{S}, \tag{2.11}$$

$$\tau_{SC} = \widetilde{SC} - \widetilde{S}\widetilde{C}, \tag{2.12}$$

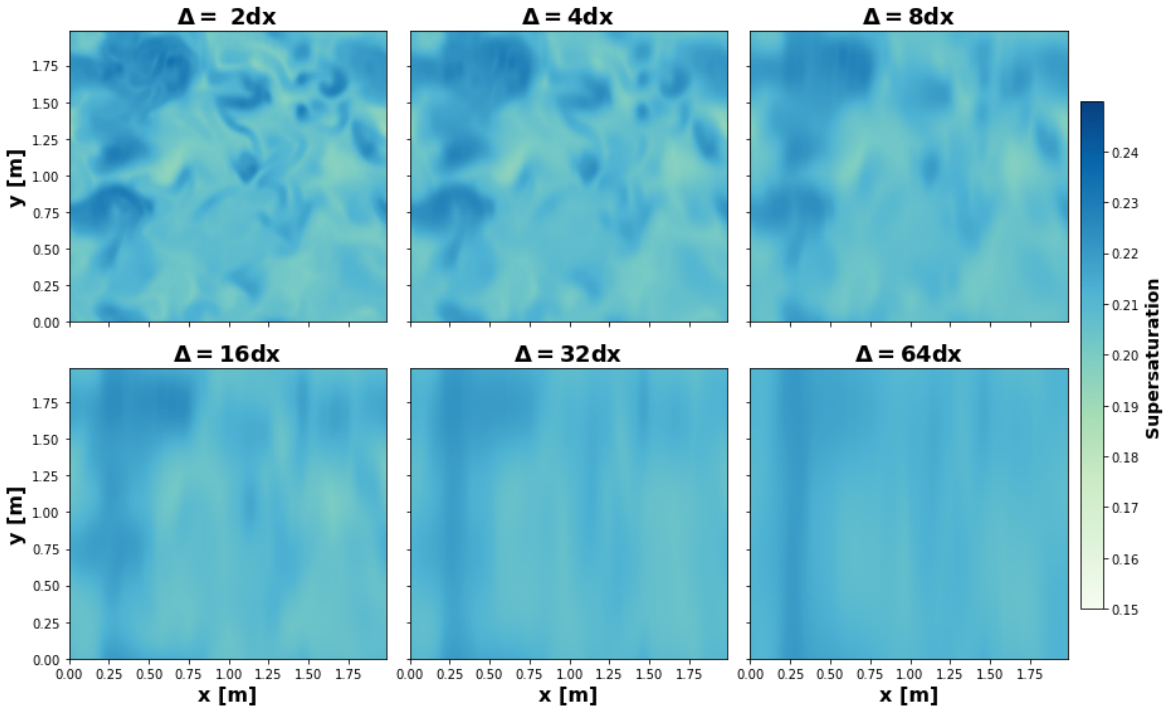

Figure 2.5: Contours of supersaturation at 0.5m for an arbitrary time where supersaturation was filtered with a 2D Gaussian filter at varying filter widths.

and

$$\tau_{CC} = \widetilde{CC} - \widetilde{C}\widetilde{C}, \tag{2.13}$$

where S is the supersaturation, C is the concentration, and $\widetilde{(\cdot)}$ represents a low-pass spatial filter. While supersaturation and concentration covariance and concentration variance are derived from equation 1.2 which evaluates the terms binned by particle size (i.e., $\chi_{s,f(r)}$ and $\chi_{f(r),f(r')}$), this study focuses on the concentration, C, of all activated particles. As noted in the introduction, the evolution equation for droplet size distribution (equ. 1.1) represents all scales of motion. To model these processes in large eddy simulations, Equation 1.1 is low pass filtered where contributions from the resolved scales and subgrid scales emerge. The contributions from the subgrid scales must be modeled in LES but do not have subgrid-scale models to represent their interactions at this time. This study will aim to develop a model for these processes.

These terms are directly related to the resolved scale quantities simulated. The supersaturation variance is important for Lagrangian models where the Langevin equation appears, while the supersaturation and concentration covariance and concentration variance terms arise within the evolution equation for droplet size distribution. As a result, representing the subgrid-scale contributions of these terms is significant for accurately simulating environments containing cloud processes. When considering subgrid scale terms containing concentration, it is important to note that those concentrations are dependent on particle size bins ($\tau_{f(r),f(r')}$). However, the number of particles in this study was limited due to a lower Rayleigh number flow. This resulted in a lack of statistical convergence for particles to be classified by particle size. Therefore, the total concentration of activated particles ($> 1\mu$m) is considered in this study. Details regarding the candidate models will be discussed in the next section.

First, the subgrid-scale terms can be broken down into resolved and modeled components:

$$\langle S'^2 \rangle = \langle \widetilde{S}'^2 \rangle + \langle \tau_{SS} \rangle. \tag{2.14}$$

Here, S is the supersaturation and $\widetilde{(\cdot)}$ represents a low-pass spatial filter and $\langle \cdot \rangle$ denotes ensemble mean. However, any subgrid scale term of interest could be replaced for supersaturation. Further, the modeled terms can be broken down into the following:

$$\tau_{SS} = \widetilde{S}\widetilde{S} - \widetilde{S}\widetilde{S}. \tag{2.15}$$

The filtered quantities in this case were calculated with a 2D Gaussian filter where $\Delta = 2$, 4, 8, 16, 32, and 64 dx. These filter widths were applied to Figure 2.5.

As expected, smaller filter widths maintain greater detail while the data becomes smoothed over with larger filter widths. Since the larger filter widths smooth out data to the point where the large-scale circulation is a challenge to distinguish, the larger

filter widths of $\Delta = 32$ and 64 dx will be neglected in this study. The filtered subgrid scale terms will be considered further in the following section.

2.3.3 Subgrid Scale Candidate Models

Once the sugbrid scale terms were calculated, further analysis into modeling the SGS terms was conducted. This study focuses on two types of models: a scale similarity model and a gradient model. These models were selected as they maintain low computational costs with test filtering for the similarity model and calculations of gradients for the gradient model. This is more efficient as compared to other methods which require solving for prognostic equations. Here, the similarity model is defined as:

$$\tau_{SS}^{m,s} = C_{sim} L_{SS},\ \tau_{SC}^{m,s} = C_{sim} L_{SC},\ \text{and}\ \tau_{CC}^{m,s} = C_{sim} L_{CC}, \tag{2.16}$$

where

$$L_{SS} = \overline{\widetilde{S}\widetilde{S}} - \overline{\widetilde{S}}\,\overline{\widetilde{S}},\ L_{SC} = \overline{\widetilde{S}\widetilde{C}} - \overline{\widetilde{S}}\,\overline{\widetilde{C}},\ \text{and}\ L_{CC} = \overline{\widetilde{C}\widetilde{C}} - \overline{\widetilde{C}}\,\overline{\widetilde{C}}, \tag{2.17}$$

is known as the Leonard term which corresponds to supersaturation variance at the smallest scales resolved in an LES, and C_{sim} represents a dimensionless coefficient that is determined by assuming that the true and modeled SGS quantities have the same mean value (i.e., $C_{sim} = \frac{\widetilde{S}'^2}{\tau_{SS}}$). In addition, the overbar terms denote test filters with a second 2D Gaussian filter with width $\overline{\Delta} = 2\Delta$ (i.e., $\overline{\Delta} = 4$, 8, 16, 32, 64, and 128 dx). Again, the last two filter widths will not be considered in this study.

In addition to the similarity model, the performance of the gradient model was also considered. It is defined as:

$$\tau_{SS}^{m,g} = C_{grad}\Delta^2 \frac{\partial \widetilde{S}}{\partial x_i}\frac{\partial \widetilde{S}}{\partial x_i},\ \tau_{SC}^{m,g} = C_{grad}\Delta^2 \frac{\partial \widetilde{S}}{\partial x_i}\frac{\partial \widetilde{C}}{\partial x_i},\ \text{and}\ \tau_{CC}^{m,g} = C_{grad}\Delta^2 \frac{\partial \widetilde{C}}{\partial x_i}\frac{\partial \widetilde{C}}{\partial x_i}, \tag{2.18}$$

where C_{grad} again represents a dimensionless coefficient. Similar to the similarity model, C_{grad} is determined by assuming that the true and modeled SGS quantities have the same mean value (i.e., $C_{sim} = \frac{\widetilde{S}'^2}{\tau_{SS}}$). Further, finite differencing was used for the vertical derivatives considering they have solid boundaries, and derivatives were taken in spectral space for the horizontal derivatives ($\frac{\partial \widetilde{S}}{\partial x}$ and $\frac{\partial \widetilde{S}}{\partial y}$) to account for the periodic domain in the horizontal directions.

Once these models were calculated, comparisons between the true and the modeled subgrid scale terms were assessed to determine the model most comparable to the true subgrid scale term. The performance of each model was assessed with statistical methods including correlation coefficients, probability density functions, and joint probability density functions. These results will be discussed in the following section. From there, conclusions could be drawn to suggest a model for further implementation into large eddy simulations.

Chapter 3

Results

This section outlines results from analysis of Pi Chamber direct numerical simulation output for the subgrid-scale (SGS) terms of interest: supersaturation variance (τ_{SS}), supersaturation and concentration covariance (τ_{SC}), and concentration variance (τ_{CC}). Each is presented with three of the five injection rate cases (the two end members and one intermediate case) and two heights (one within the bulk of the flow, and one within the upper boundary layer) as strong trends correlating to injection rates and heights were not observed. Both candidate models (scale-similarity and gradient models) were assessed with statistical analysis including probability density functions, joint probability density functions, and correlation coefficients.

3.1 Supersaturation Variance

This section investigates the SGS model performance for the supersaturation variance (τ_{SS}). First, the SGS fraction was considered (Fig. 3.1). This is the fraction of the SGS supersaturation variance to the total resolved plus SGS supersaturation variance. The SGS fraction was assessed at three different injection rates ($\dot{n}$ = 1, 10, and 100 $\mathrm{cm}^{-3}\,\mathrm{min}^{-1}$) and four varying filter widths (Δ/dx = 2, 4, 8, and 16). For smaller filter widths (Δ/dx = 2 or 4), more than 50% of the supersaturation variance was resolved at the grid level. When considering larger filter widths (Δ/dx = 8 or 16), more than

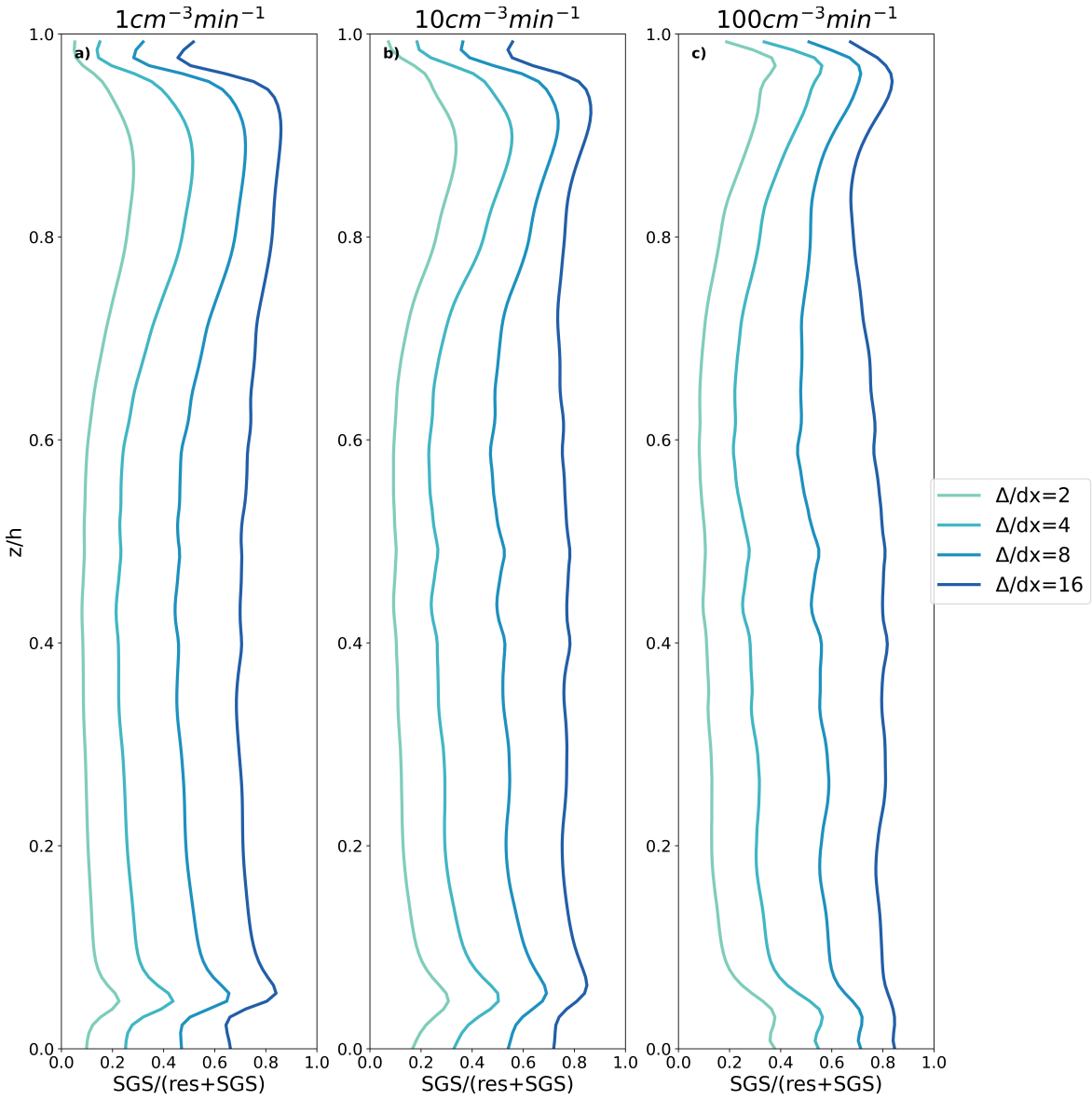

Figure 3.1: SGS fraction of the supersaturation variance with height at varying filter widths and injection rates.

50% of the supersaturation variance remained in the sub-grid scales which must be modeled. Despite some variability in the bottom and top boundaries, there were few differences between each injection rate case.

The probability density functions (PDFs) were analyzed for the true SGS supersaturation variance (τ_{SS}) and both candidate models (gradient model, $\tau_{SS}^{m,g}$, and similarity

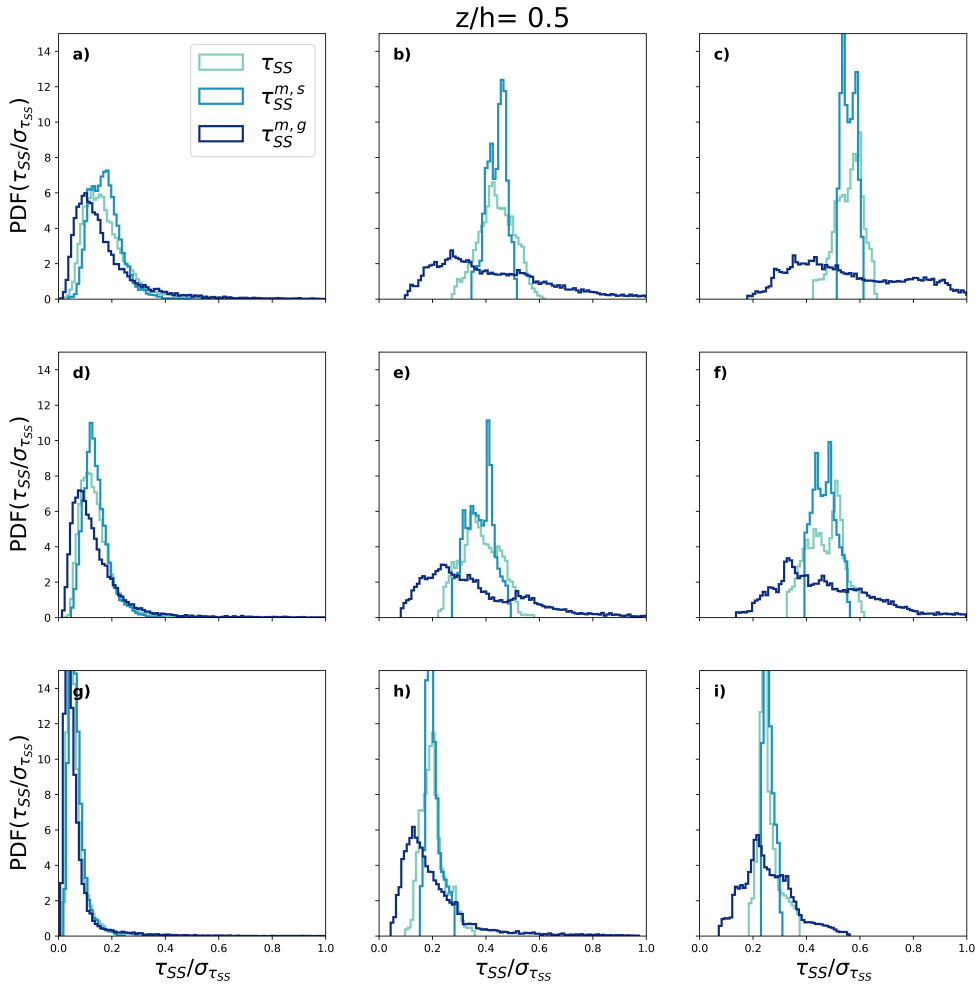

Figure 3.2: Probability density functions of the true SGS supersaturation variance (τ_{SS}) and modeled supersaturation variance for the similarity model ($\tau_{SS}^{m,s}$) and the gradient model ($\tau_{SS}^{m,g}$) normalized by the standard deviation of the true SGS term ($\sigma_{\tau_{SS}}$). All are plotted at one height (z/h=0.5) within the bulk of the flow. The injection rate increases from top to bottom: $\dot{n}$ = 1 (a-c), 10 (d-f), and 100 (g-i) cm^{-3} min^{-1}. The filter width increases from left to right: Δ/dx= 2 (a, d, g), 8 (b, e, h), and 16 (c, f, i).

model $\tau_{SS}^{m,s}$). All were normalized by the standard deviation of the true subgrid supersaturation variance ($\sigma_{\tau_{SS}}$). These PDFs were evaluated with increasing aerosol injection rates ($\dot{n}$ = 1, 10, and 100 cm^{-3} min^{-1}), increasing filter widths (Δ/dx = 2,

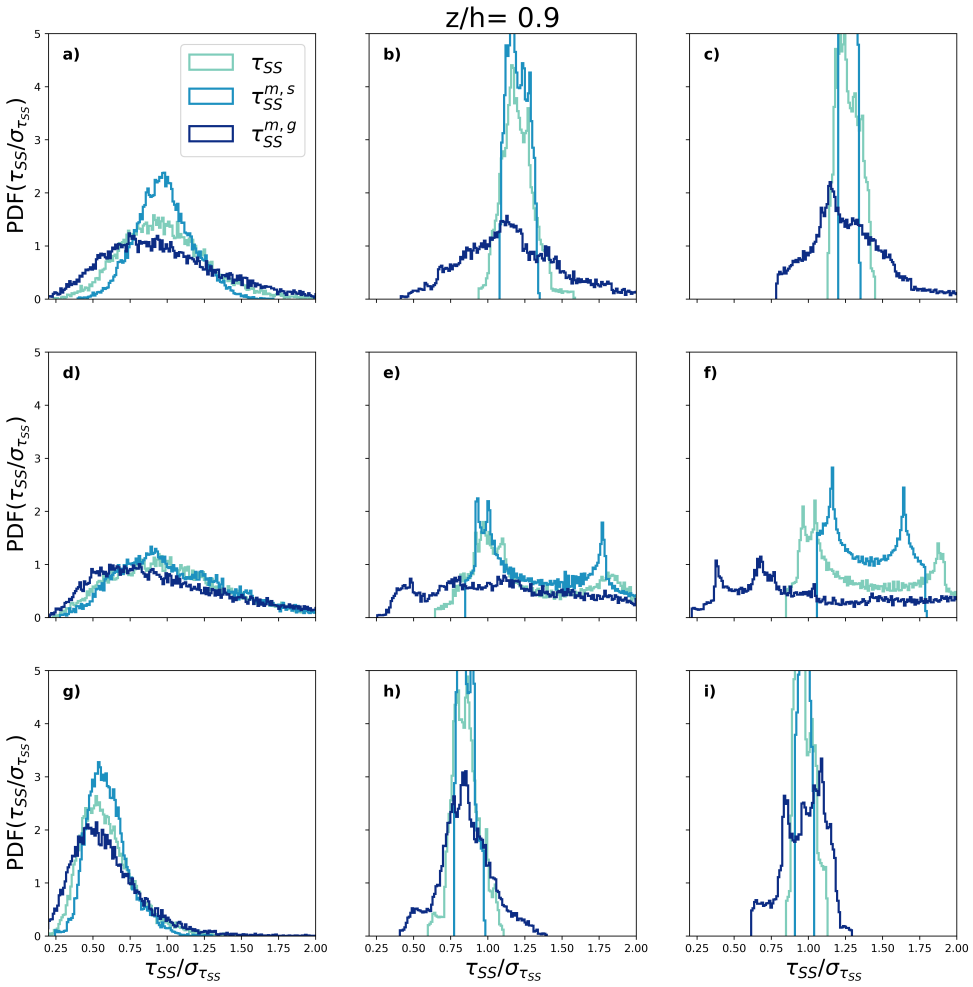

Figure 3.3: Probability density functions of the true SGS supersaturation variance (τ_{SS}) and modeled supersaturation variance for the similarity model ($\tau_{SS}^{m,s}$) and the gradient model ($\tau_{SS}^{m,g}$) normalized by the standard deviation of the true SGS term ($\sigma_{\tau_{SS}}$). All are plotted at one height (z/h=0.9) near the upper boundary layer. The injection rate increases from top to bottom: $\dot{n} = 1$ (a-c), 10 (d-f), and 100 (g-i) $\mathrm{cm}^{-3}\,\mathrm{min}^{-1}$. The filter width increases from left to right: Δ/dx= 2 (a, d, g), 8 (b, e, h), and 16 (c, f, i).

8, and 16), and at two locations: one within the bulk of the flow (z/h= 0.5, Fig. 3.2) and one within the upper boundary layer (z/h= 0.9, Fig. 3.3). There were gamma distributions for the smallest filter widths (Figures 3.2 and 3.3 (a), (d), and (g)) with

a transition to a nearly bimodal distribution at the largest filter widths (Figures 3.2 and 3.3 (d), (f), and (i)). The transition to a bimodal distribution was likely due to increasing filter width where the large-scale circulation characteristic of Rayleigh-Bénard convection influenced the PDFs. This bimodal feature was particularly noted in the injection rate case $\dot{n} = 10\text{cm}^{-3}\,\text{min}^{-1}$ (Figures 3.2 and 3.3 d-f). It is uncertain why this injection rate produces these results as compared to the others.

When assessing the trends of each candidate model, there were significant discrepancies observed. While both the gradient and similarity models closely followed the true SGS supersaturation variance for the smallest filter width $\Delta/dx = 2$, the gradient model quickly underpredicted the PDFs at the larger filter widths. In contrast, the similarity model more closely represented the trends observed in the true SGS supersaturation variance across all filter widths, injection rates, and heights. However, it is important to note that the PDFs only provide information about the distributions in the mean sense; PFDs do not provide information as to whether the true and modeled SGS terms are correlated. As such, joint PDFs and correlation coefficients are analyzed for each candidate model in the following sections.

3.1.1 Gradient Model

First, the gradient model was evaluated using joint PDFs for the same injection rates ($\dot{n}$ = 1, 10, and 100 $\text{cm}^{-3}\,\text{min}^{-1}$), filter widths ($\Delta/dx$ = 2, 8, and 16), and heights (z/h= 0.5 and 115) as the PDFs previously discussed (figures 3.4 and 3.5). Consistent with the hypothesized results from the PDFs, the joint PDFs were not well aligned with the one-to-one line that indicates good agreement between the true SGS supersaturation variance, τ_{SS}, and the modeled supersaturation variance, $\tau_{SS}^{m,g}$. Overall, it did

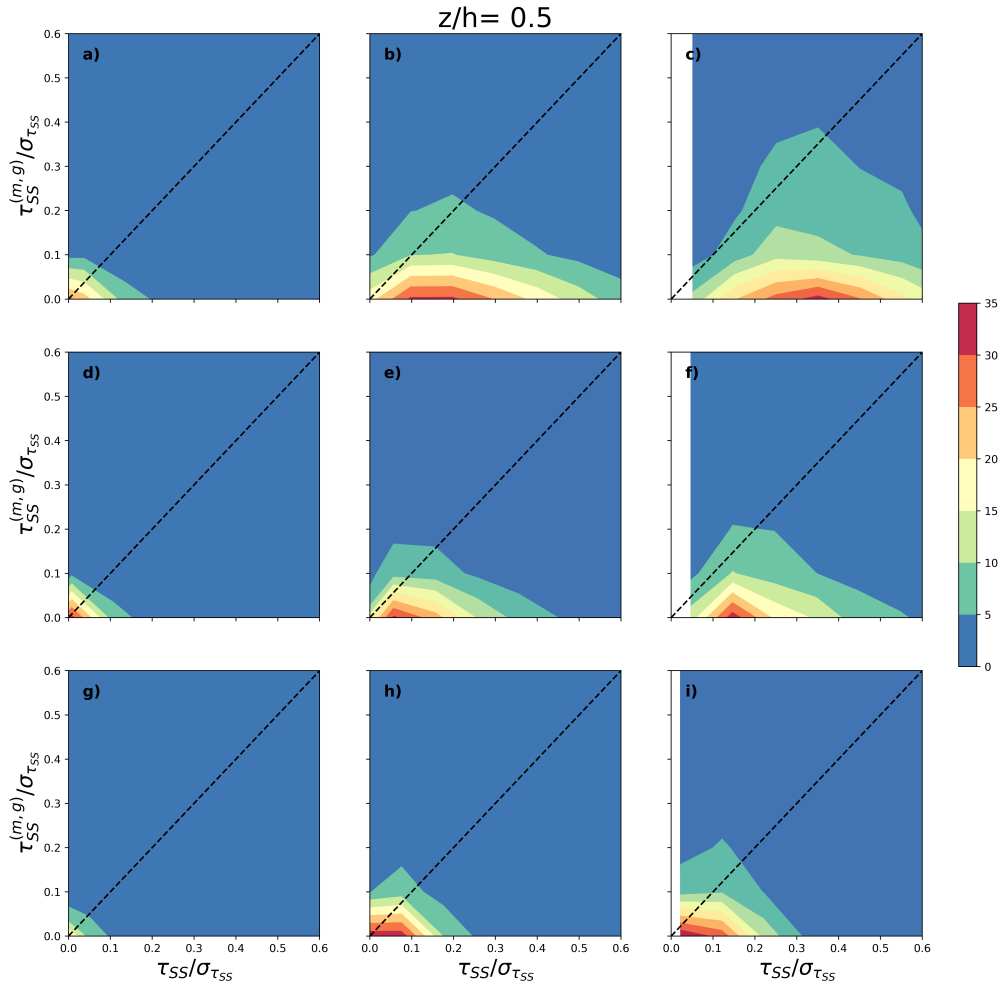

Figure 3.4: Joint probability density functions of the true SGS supersaturation variance (τ_{SS}) and modeled supersaturation variance for the gradient model ($\tau_{SS}^{m,g}$) normalized by the standard deviation of the true SGS term ($\sigma_{\tau_{SS}}$). All are plotted at one height (z/h=0.5) within the bulk of the flow. The injection rate increases from top to bottom: $\dot{n}$ = 1 (a-c), 10 (d-f), and 100 (g-i) $\mathrm{cm}^{-3}\,\mathrm{min}^{-1}$. The filter width increases from left to right: Δ/dx= 2 (a, d, g), 8 (b, e, h), and 16 (c, f, i).

not appear that changes in the injection rates or filter widths produced significantly different results. However, greater variability appeared within the upper boundary

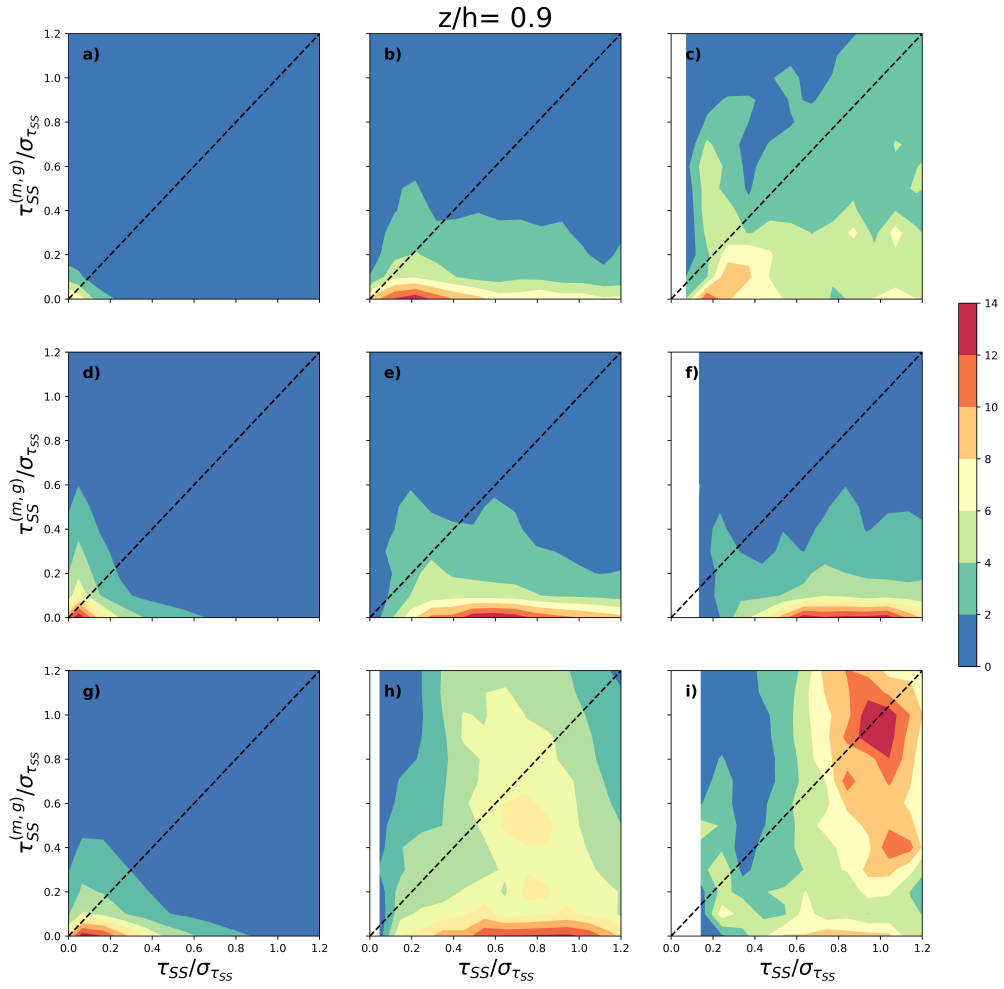

Figure 3.5: Joint probability density functions of the true SGS supersaturation variance (τ_{SS}) and modeled supersaturation variance for the gradient model ($\tau_{SS}^{m,g}$) normalized by the standard deviation of the true SGS term ($\sigma_{\tau_{SS}}$). All are plotted at one height (z/h=0.9) near the upper boundary layer. The injection rate increases from top to bottom: $\dot{n}$ = 1 (a-c), 10 (d-f), and 100 (g-i) $\mathrm{cm}^{-3}\,\mathrm{min}^{-1}$. The filter width increases from left to right: Δ/dx= 2 (a, d, g), 8 (b, e, h), and 16 (c, f, i).

layer (Fig. 3.5) as compared to the bulk of the flow (Fig. 3.4). This variability did not result in better performance of the gradient model.

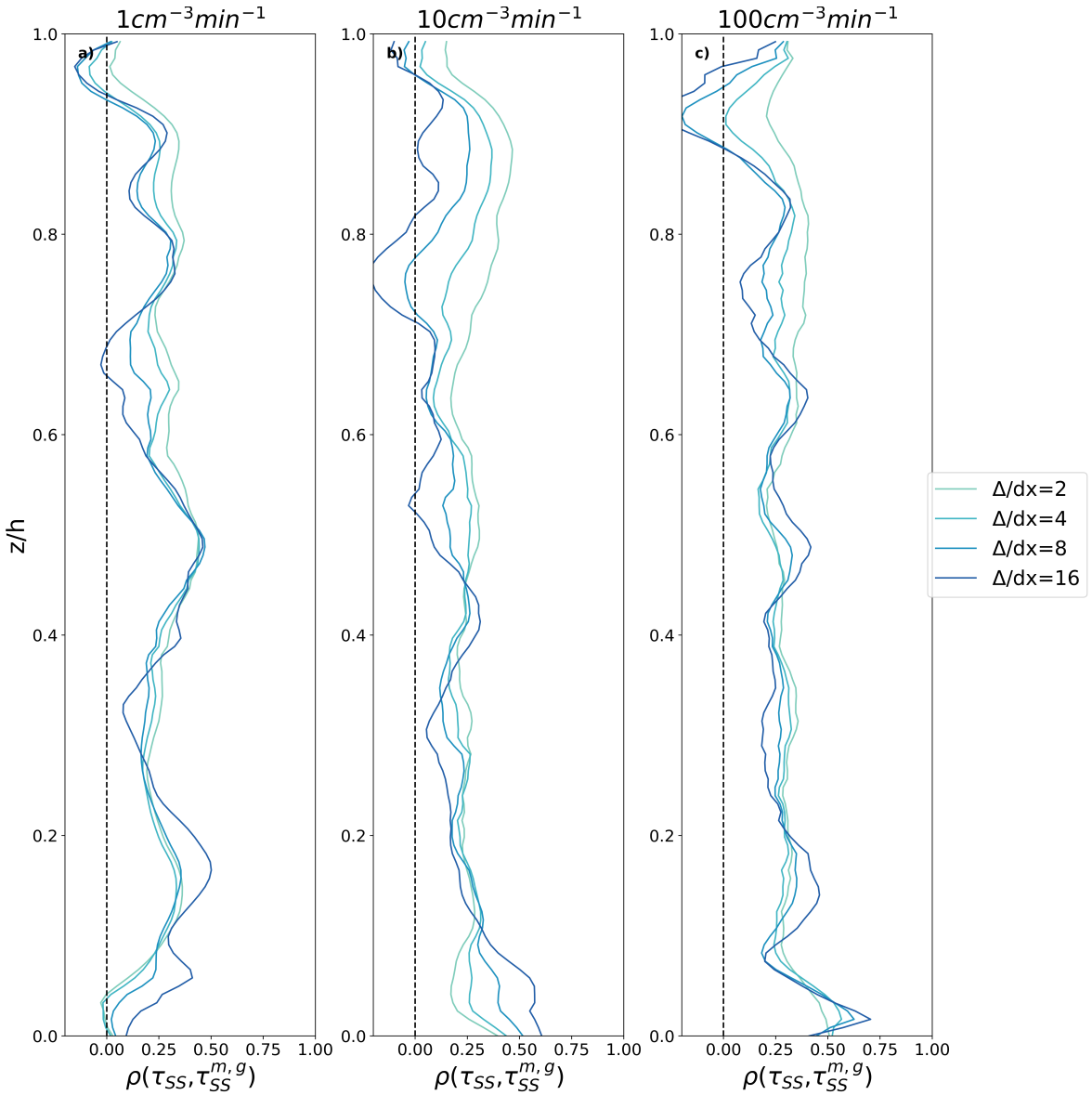

Figure 3.6: Correlation coefficients of the true SGS supersaturation variance (τ_{SS}) and modeled supersaturation variance for the gradient model ($\tau_{SS}^{m,g}$) with height at varying filter widths and injection rates.

Further supporting the conclusions that the gradient model doesn't represent the true SGS supersaturation variance well were the correlation coefficients presented in Figure 3.6. These are plotted for the three injection rates considered previously in addition to four filter widths ($\Delta/dx = 2$, 4, 8, and 16). While the correlation coefficients

were not constant with height, they were generally between $\rho \approx 0.1 - 0.4$ (Fig. 3.6). There were no clear differences in the correlation coefficients between injection rates. However, there were some differences in the correlation coefficients at varying filter widths. Overall, the correlation coefficients of the filter widths oscillated around $\rho \approx 0.1 - 0.4$, but the larger filter widths ($\Delta/dx = 8$ and 16) had greater fluctuations toward lower ρ values. Despite this, the general statement remains true that the gradient model had little skill in modeling the true SGS supersaturation variance. Further discussion of this will take place in Section 3.1.3.

3.1.2 Similarity Model

Consistent with the gradient model, joint PDFs were investigated for the true SGS supersaturation variance (τ_{SS}) and modeled supersaturation variance with the similarity model ($\tau_{SS}^{m,s}$). In analyzing these across varying injection rates ($\dot{n}$ = 1, 10, and 100 $\mathrm{cm}^{-3}\,\mathrm{min}^{-1}$), filter widths ($\Delta/dx$ = 2, 8, and 16), and heights (z/h= 65 and 115), the similarity mode closely followed the one-to-one line indicating good agreement between the true and modeled SGS supersaturation variance (figures 3.7 and 3.8). However, the joint PDFs were slightly above this line suggesting the model may slightly overpredict the true SGS supersaturation variance. These observations followed closely across all injection rates, filter widths, and the two heights selected.

When considering the correlation coefficients for each of these injection rates and filter widths (Δ/dx = 2, 4, 8, and 16), there was surprising agreement across all cases. The correlation coefficients were nearly always between ρ = 0.75-0.9, suggesting a good correlation between the true and modeled SGS supersaturation variance (Fig. 3.9). In addition, this was consistent across all filter widths. There was some variability at

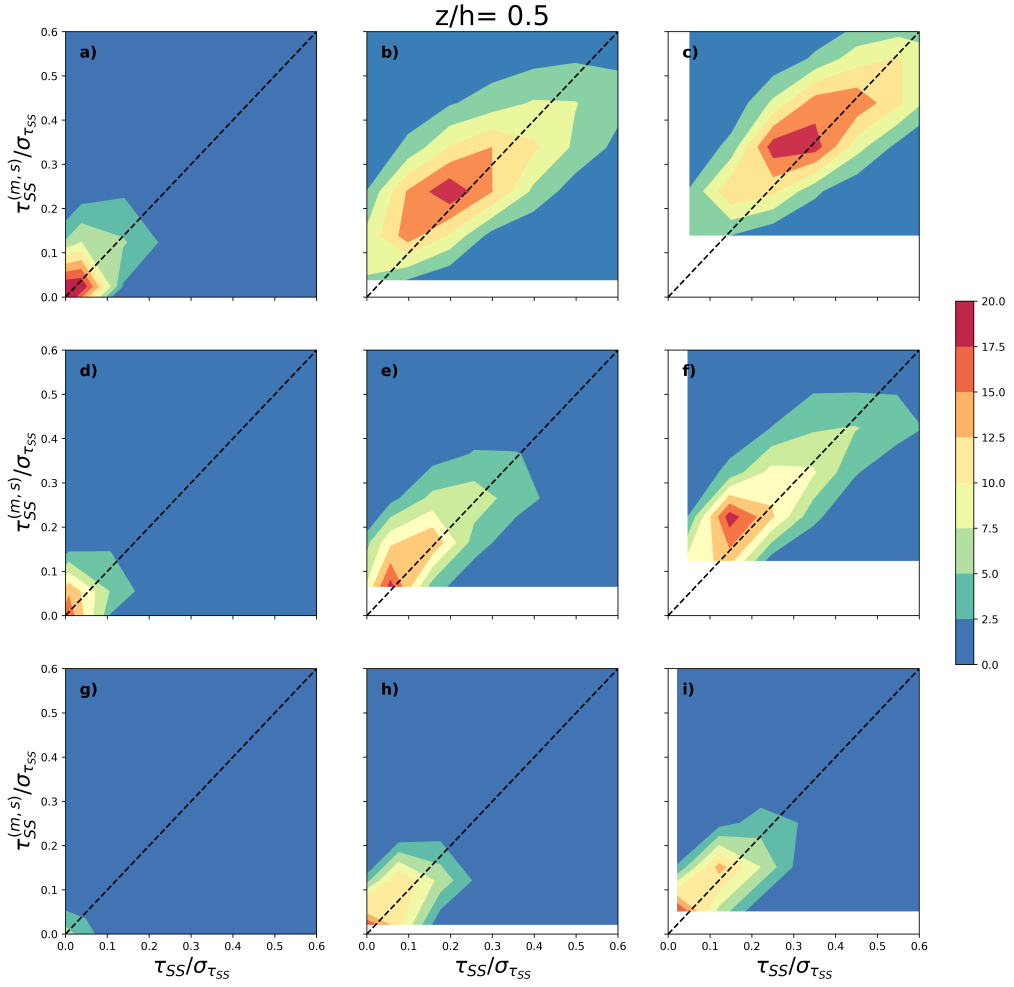

Figure 3.7: Joint probability density functions of the true SGS supersaturation variance (τ_{SS}) and modeled supersaturation variance for the similarity model ($\tau_{SS}^{m,s}$) normalized by the standard deviation of the true SGS term ($\sigma_{\tau_{SS}}$). All are plotted at one height (z/h=0.5) within the bulk of the flow. The injection rate increases from top to bottom: $\dot{n}$ = 1 (a-c), 10 (d-f), and 100 (g-i) cm^{-3} min^{-1}. The filter width increases from left to right: Δ/dx= 2 (a, d, g), 8 (b, e, h), and 16 (c, f, i).

$\Delta/dx = 16$, but the variability that occurred was not significant or indicative of little correlation between the true and modeled terms. It is also worth noting that the correlation remained high throughout the profile, despite changes in the SGS fraction

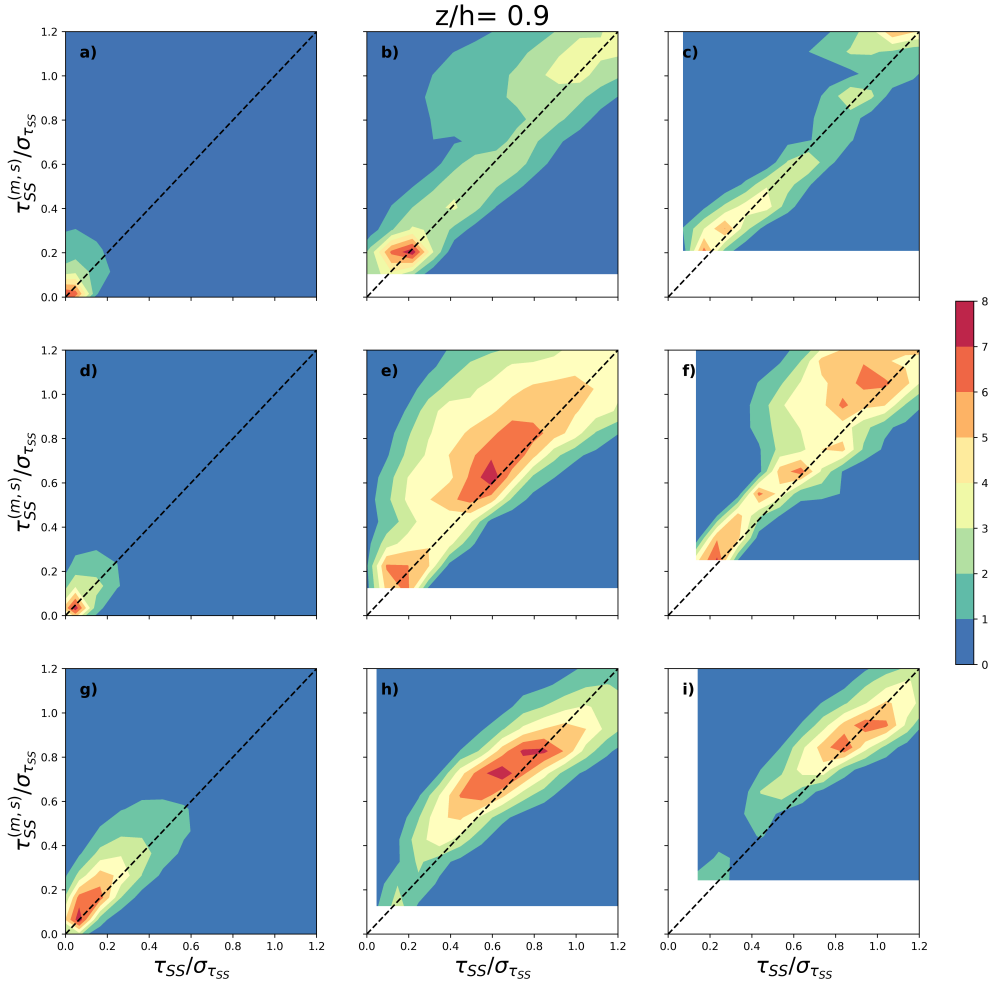

Figure 3.8: Joint probability density functions of the true SGS supersaturation variance (τ_{SS}) and modeled supersaturation variance for the similarity model ($\tau_{SS}^{m,s}$) normalized by the standard deviation of the true SGS term ($\sigma_{\tau_{SS}}$). All are plotted at one height (z/h=0.9) near the upper boundary layer. The injection rate increases from top to bottom: $\dot{n}$ = 1 (a-c), 10 (d-f), and 100 (g-i) cm^{-3} min^{-1}. The filter width increases from left to right: Δ/dx= 2 (a, d, g), 8 (b, e, h), and 16 (c, f, i).

due to the bottom and top boundary layer features. Overall, this model performed well throughout the profile, at varying injection rates, and filter widths.

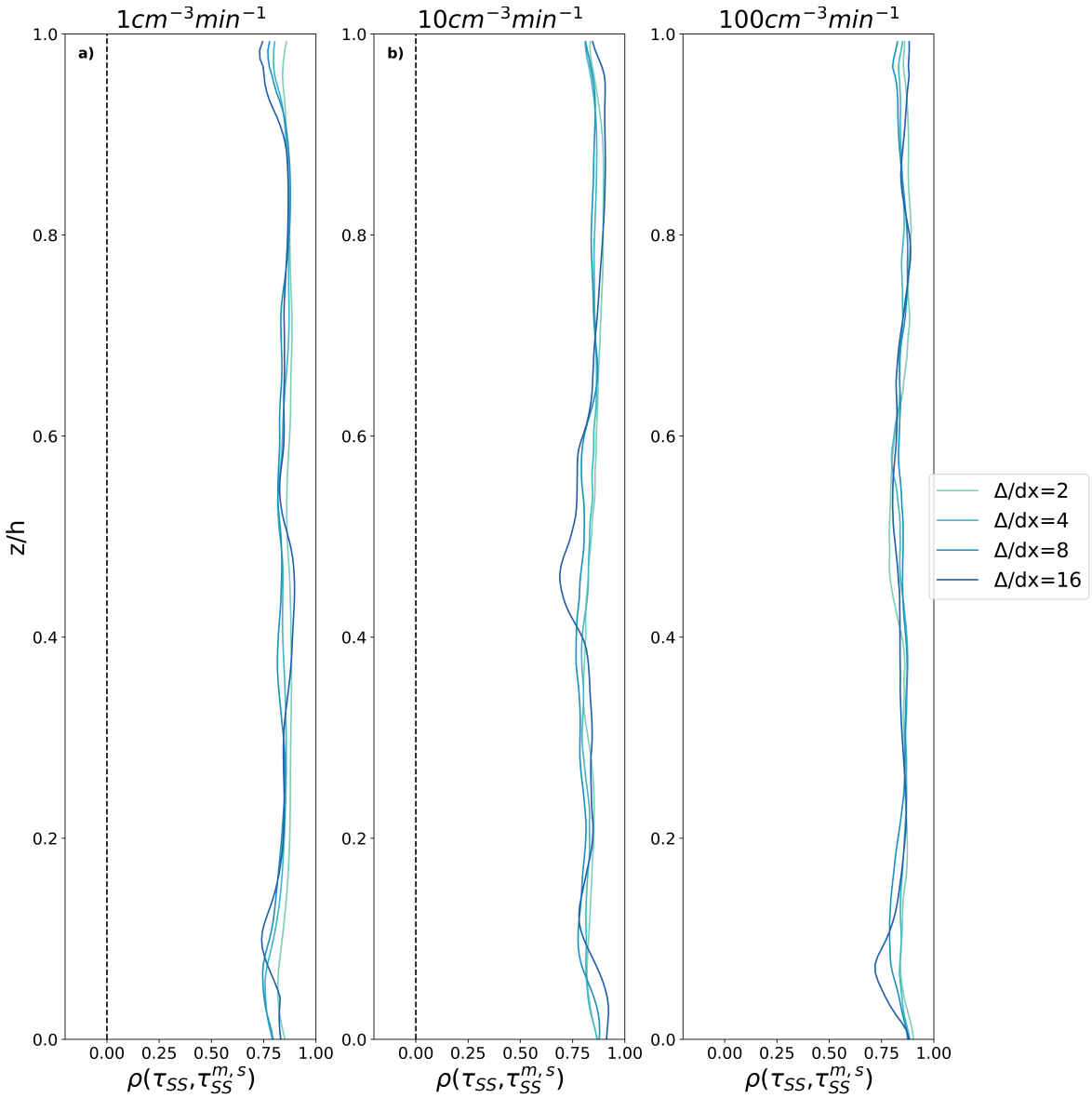

Figure 3.9: Correlation coefficients of the true SGS supersaturation variance (τ_{SS}) and modeled supersaturation variance for the similarity model ($\tau_{SS}^{m,s}$) with height at varying filter widths and injection rates.

3.1.3 Discussion

Both the gradient and similarity models were assessed with PDFs, joint PDFs, and correlation coefficients to identify the utility of either model for representing the SGS supersaturation variance. Results suggest that the gradient model was less skillful at

modeling this term as the PDFs do not replicate the true SGS supersaturation variance PDFs, joint PDFs deviate significantly from the one-to-one line, and low values for correlation coefficient were observed. In contrast, the PDFs of the similarity model replicated those of the true SGS supersaturation variance. Further, the joint PDFs of the similarity model showed trends that closely followed the one-to-one line indicative of positive agreement between the true and modeled SGS supersaturation variance. Correlation coefficients generally greater than $\rho = 0.75$ also indicated good correlation between these cases. This agreement was observed for each filter width suggesting that any filter width chosen for an SGS model will have skill in representing the SGS supersaturation variance. Considering the similarity model performs well for large filter widths (i.e., $\Delta/dx = 8$ or 16), it has practical relevance for modeling cloud-containing environments with large eddy simulations of moderate resolution.

3.2 Supersaturation and Concentration Covariance

To remain consistent with the supersaturation variance, profiles for the SGS fraction of concentration covariance were evaluated at varying injection rates ($\dot{n}$ = 1, 10, and 100 $\mathrm{cm^{-3}\,min^{-1}}$) and filter widths ($\Delta/dx$ = 2, 4, 8, and 16, Fig. 3.10). Similar to the results of supersaturation variance, the supersaturation and concentration covariance generally remained less than 50% indicating that the majority of the SGS covariance is located on the resolved scale. However, this did not apply when considering the larger filter widths ($\Delta/dx = 8$ or 16) at the transition between the boundary layer features and the bulk of the flow. Here, the SGS fraction was between approximately 60-90%, excluding the upper boundary layer for the 100 $\mathrm{cm^{-3}\,min^{-1}}$ case, and $\Delta/dx = 8$ for the 10 $\mathrm{cm^{-3}\,min^{-1}}$ case at the lower boundary layer. In general, the SGS fraction between

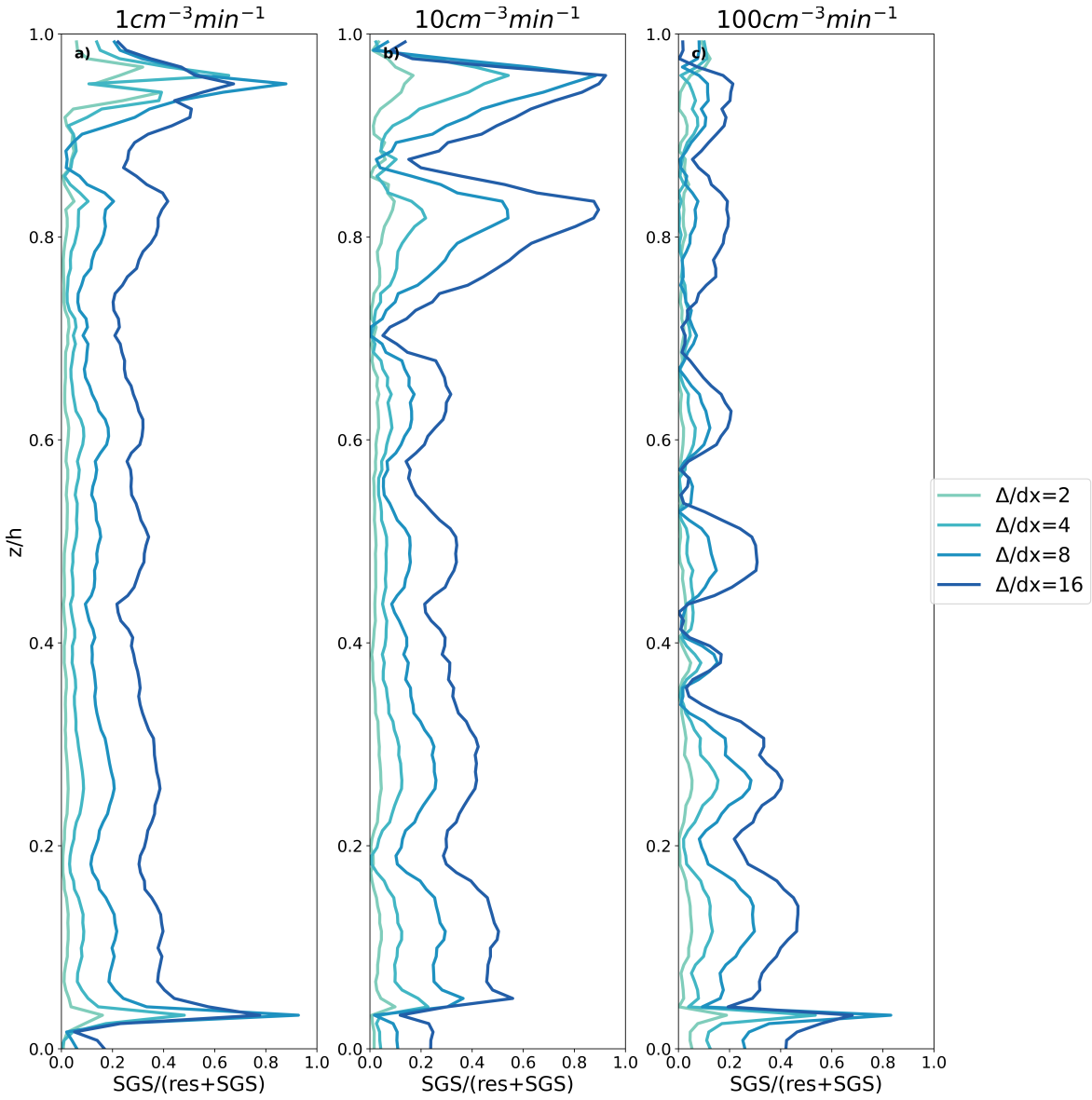

Figure 3.10: SGS fraction of the supersaturation and concentration covariance with height at varying filter widths and injection rates.

60-90% suggests that the transition between the boundary layers and the bulk of the flow primarily occurs within the subgrid scales. Overall, larger filter widths resulted in a higher percentage of the supersaturation and concentration covariance located in the subgrid scales. Otherwise, there were no significant differences between each case.

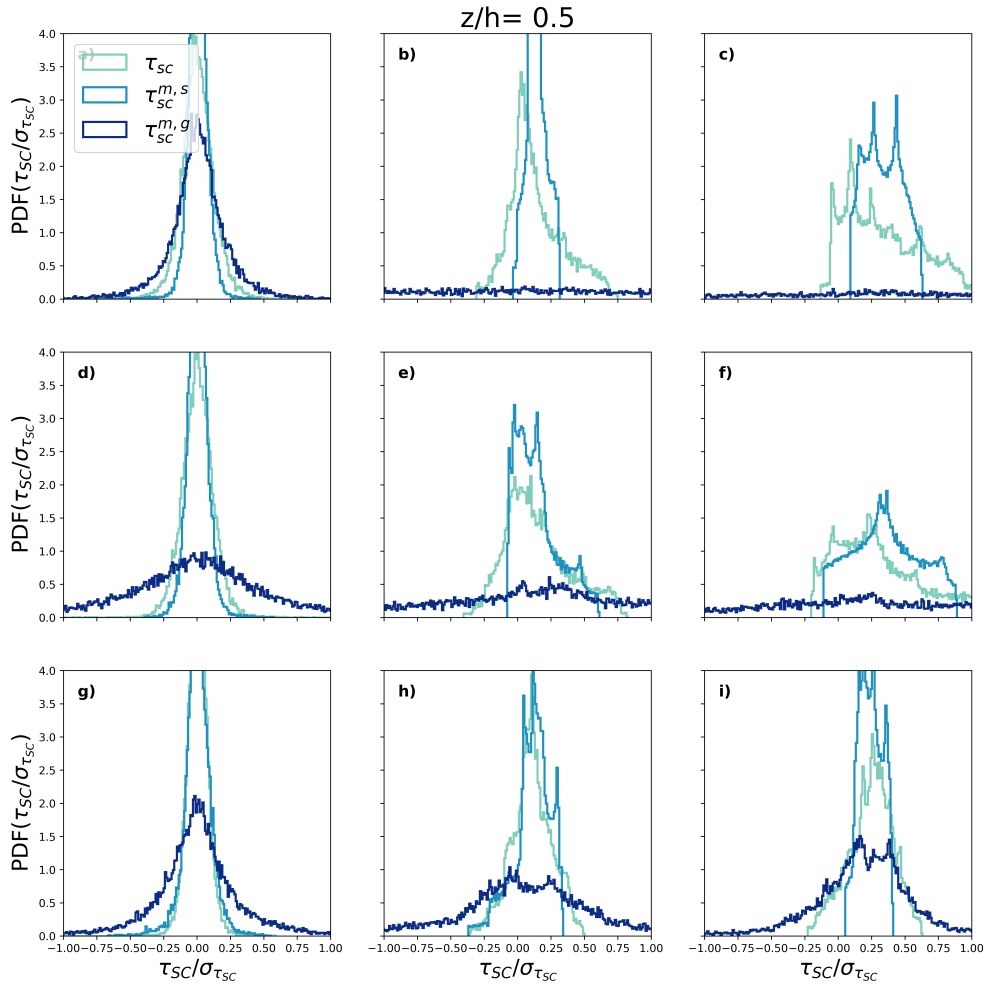

Figure 3.11: Probability density functions of the true SGS supersaturation and concentration covariance (τ_{SC}) and modeled supersaturation and concentration covariance for the similarity model ($\tau_{SC}^{m,s}$) and the gradient model ($\tau_{SC}^{m,g}$) normalized by the standard deviation of the true SGS term ($\sigma_{\tau_{SC}}$). All are plotted at one height (z/h=0.5) within the bulk of the flow. The injection rate increases from top to bottom: $\dot{n} = 1$ (a-c), 10 (d-f), and 100 (g-i) $\mathrm{cm}^{-3}\,\mathrm{min}^{-1}$. The filter width increases from left to right: Δ/dx= 2 (a, d, g), 8 (b, e, h), and 16 (c, f, i).

PDFs of the supersaturation and concentration covariance for the true SGS covariance (τ_{SS}), gradient-modeled SGS covariance ($\tau_{SS}^{m,g}$), and similarity-modeled SGS

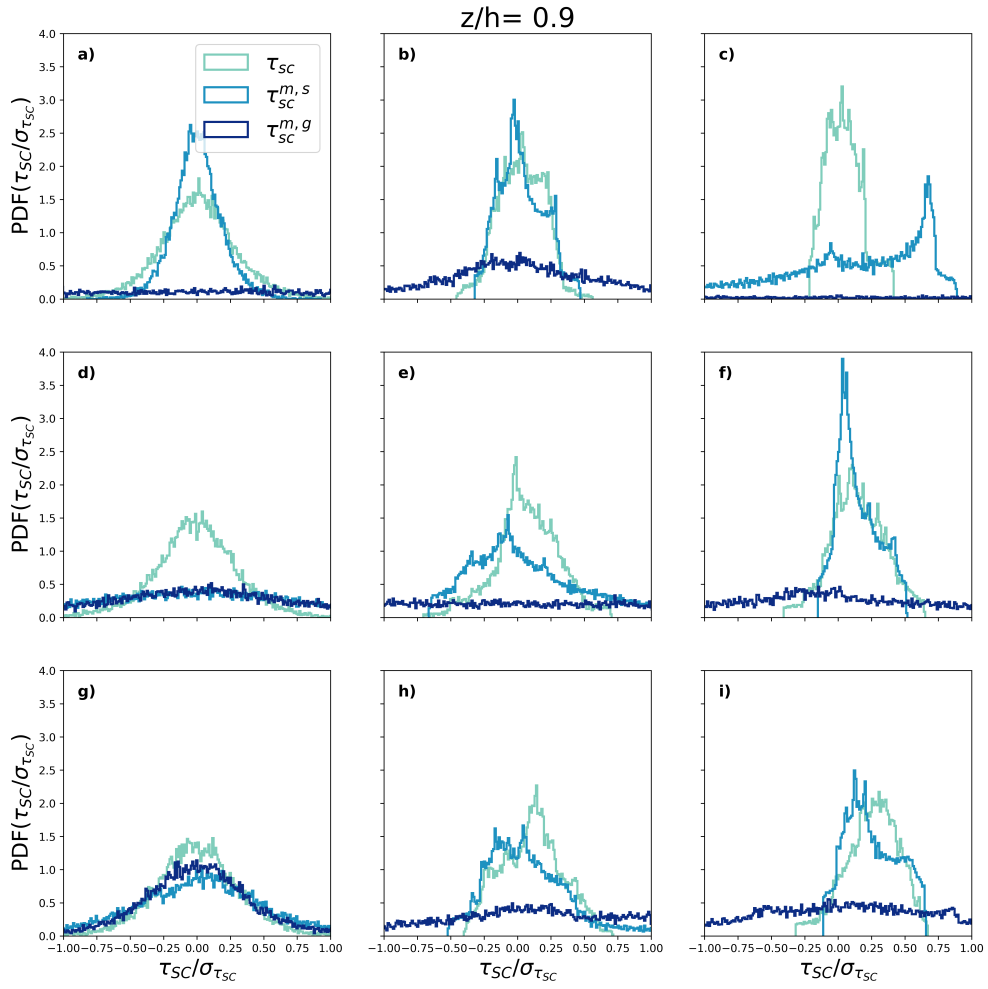

Figure 3.12: Probability density functions of the true SGS supersaturation and concentration covariance (τ_{SC}) and modeled supersaturation and concentration covariance for the similarity model ($\tau_{SC}^{m,s}$) and the gradient model ($\tau_{SC}^{m,g}$) normalized by the standard deviation of the true SGS term ($\sigma_{\tau_{SC}}$). All are plotted at one height (z/h=0.9) near the upper boundary layer. The injection rate increases from top to bottom: $\dot{n} = 1$ (a-c), 10 (d-f), and 100 (g-i) $\mathrm{cm}^{-3}\,\mathrm{min}^{-1}$. The filter width increases from left to right: Δ/dx= 2 (a, d, g), 8 (b, e, h), and 16 (c, f, i).

covariance ($\tau_{SS}^{m,s}$) were compared between different filter widths ($\Delta/dx = 2$, 8, and 16) and injection rates ($\dot{n} = 1$, 10, and 100 $\mathrm{cm}^{-3}\,\mathrm{min}^{-1}$) at two heights: z/h= 0.5 and z/h=

0.9 (Figures 3.11 and 3.12). Similar to supersaturation variance, these PDFs appeared near Gaussian with smaller filter widths and transitioned to a bimodal distribution for larger filter widths. As noted previously, this bimodal distribution likely occurred due to influences of the large-scale circulation. In assessing each injection rate, trends in the results remained relatively consistent across all cases. However, there were considerable differences when evaluating the difference between the true and modeled SGS supersaturation and concentration covariance.

Similar to the supersaturation variance, the similarity model produced PDFs that followed the same trend as the true SGS supersaturation and concentration covariance. However, there were a few exceptions to this, particularly within the upper boundary layer where there were outliers (Fig. 3.12 (c) and (d)). However, the gradient model displayed little skill in capturing the trends of the PDFs throughout all cases. Since definitive results regarding the skill of models could not be assessed with the SGS fraction and PDFs, these will be quantified further in the following section.

3.2.1 Gradient Model

Joint PDFs of the gradient model ($\tau_{SC}^{m,g}$) and true SGS supersaturation and concentration covariance (τ_{SC}) for the cases described for the PDFs in the previous section are presented in Figures 3.13 and 3.14. The results are consistent across all injection rates, filter widths, and heights. None of the joint PDFs for the given cases aligned closely about the one-to-one line that would suggest positive agreement between the true and modeled SGS supersaturation and concentration covariance. This suggests little skill in using the gradient model to represent this term.

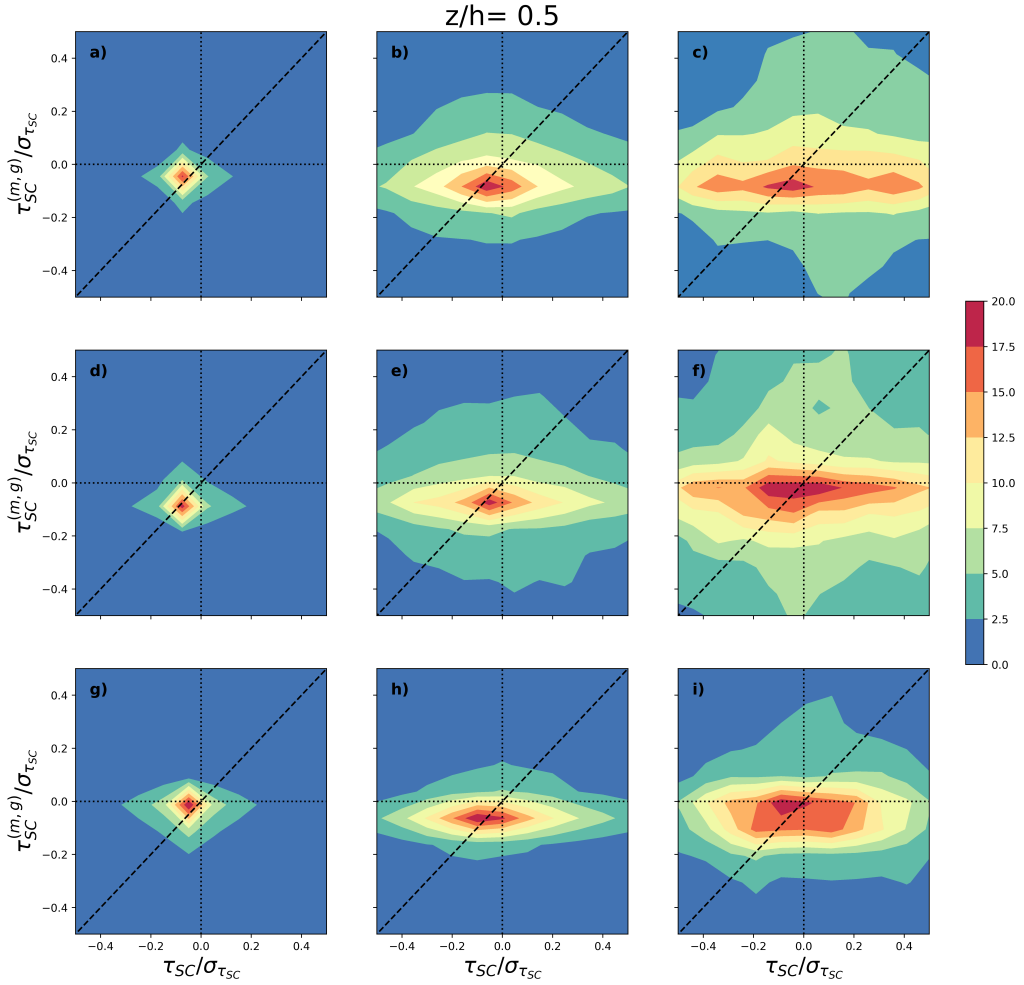

Figure 3.13: Joint probability density functions of the true SGS supersaturation and concentration covariance (τ_{SC}) and modeled supersaturation and concentration covariance for the gradient model ($\tau_{SC}^{m,g}$) normalized by the standard deviation of the true SGS term ($\sigma_{\tau_{SC}}$). All are plotted at one height (z/h=0.5) within the bulk of the flow. The injection rate increases from top to bottom: $\dot{n}$ = 1 (a-c), 10 (d-f), and 100 (g-i) $\mathrm{cm}^{-3}\,\mathrm{min}^{-1}$. The filter width increases from left to right: Δ/dx= 2 (a, d, g), 8 (b, e, h), and 16 (c, f, i).

Supporting this conclusion were the correlation coefficients between the gradient modeled and true SGS supersaturation and concentration covariance (Fig. 3.15). For

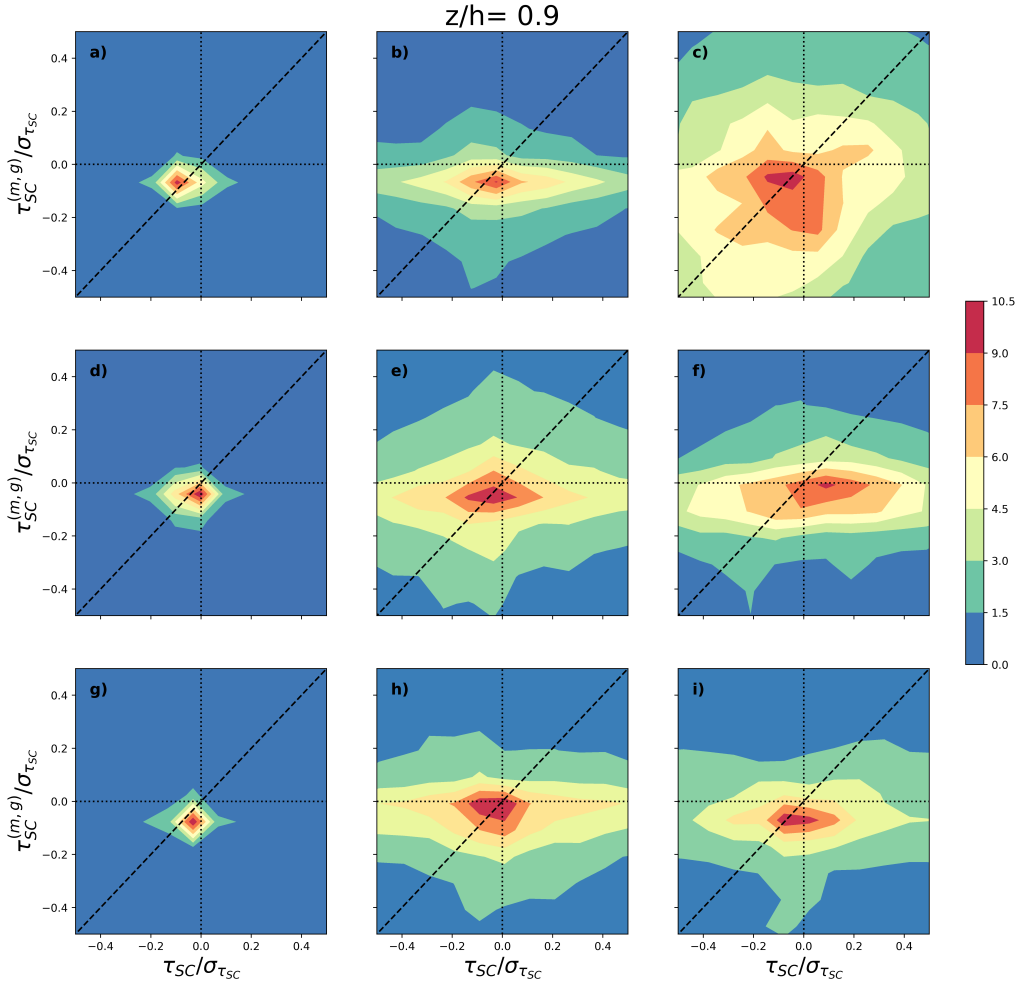

Figure 3.14: Joint probability density functions of the true SGS supersaturation and concentration covariance (τ_{SC}) and modeled supersaturation and concentration covariance for the gradient model ($\tau_{SC}^{m,g}$) normalized by the standard deviation of the true SGS term ($\sigma_{\tau_{SC}}$). All are plotted at one height (z/h=0.9) near the upper boundary layer. The injection rate increases from top to bottom: $\dot{n} = 1$ (a-c), 10 (d-f), and 100 (g-i) $\mathrm{cm}^{-3}\,\mathrm{min}^{-1}$. The filter width increases from left to right: Δ/dx= 2 (a, d, g), 8 (b, e, h), and 16 (c, f, i).

each injection rate and filter width, the correlation coefficients oscillated about $\rho = 0$ throughout the profile. This indicates no correlation between the true and modeled

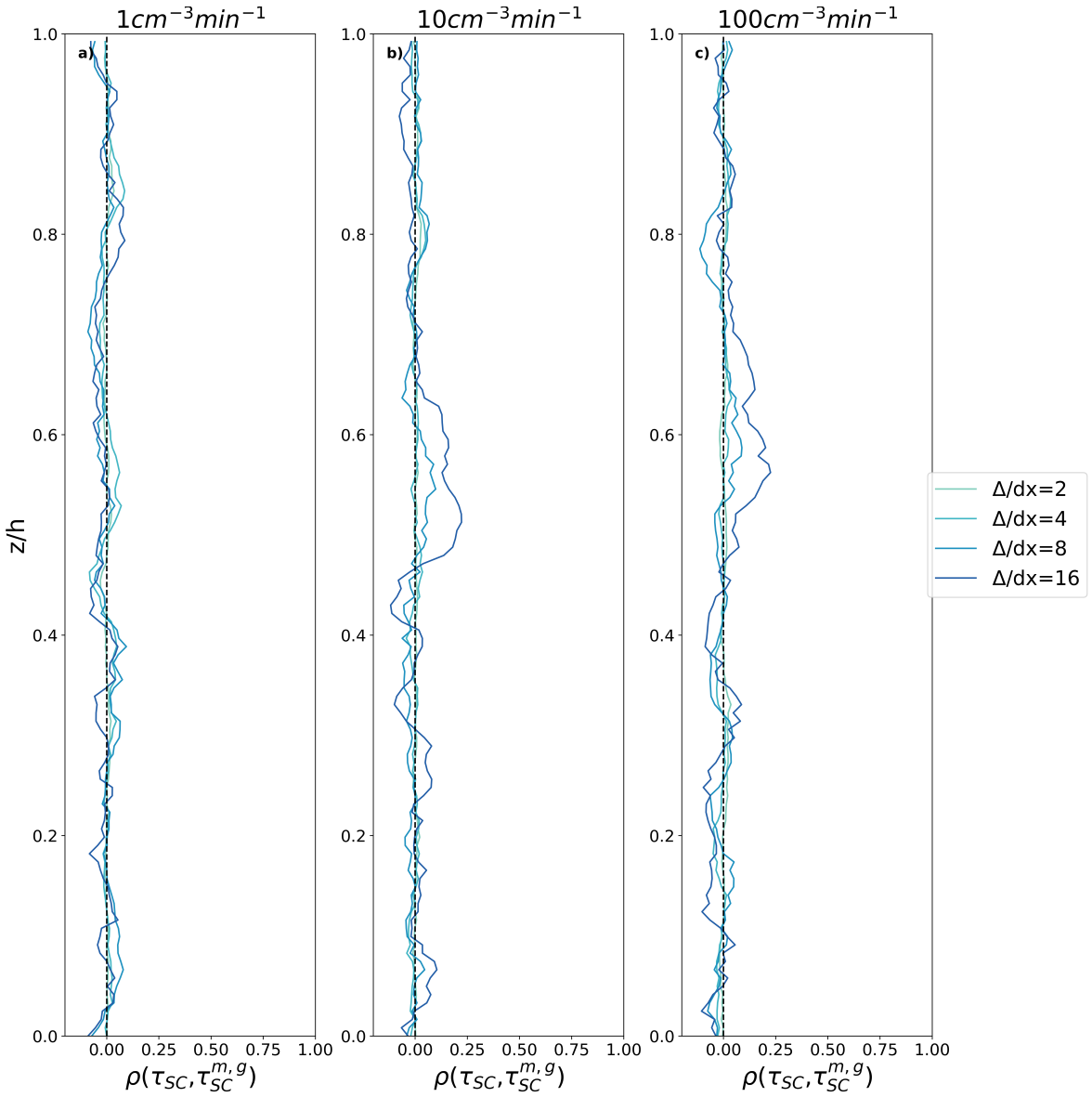

Figure 3.15: Correlation coefficients of the true SGS supersaturation and concentration covariance (τ_{SC}) and modeled supersaturation and concentration variance for the gradient model ($\tau_{SC}^{m,g}$) with height at varying filter widths and injection rates.

SGS supersaturation and concentration covariance. In addition, it did not appear that a particular injection rate or filter width improves the correlation coefficients produced. As a result, the gradient model is not recommended to represent the SGS supersaturation and concentration covariance.

3.2.2 Similarity Model

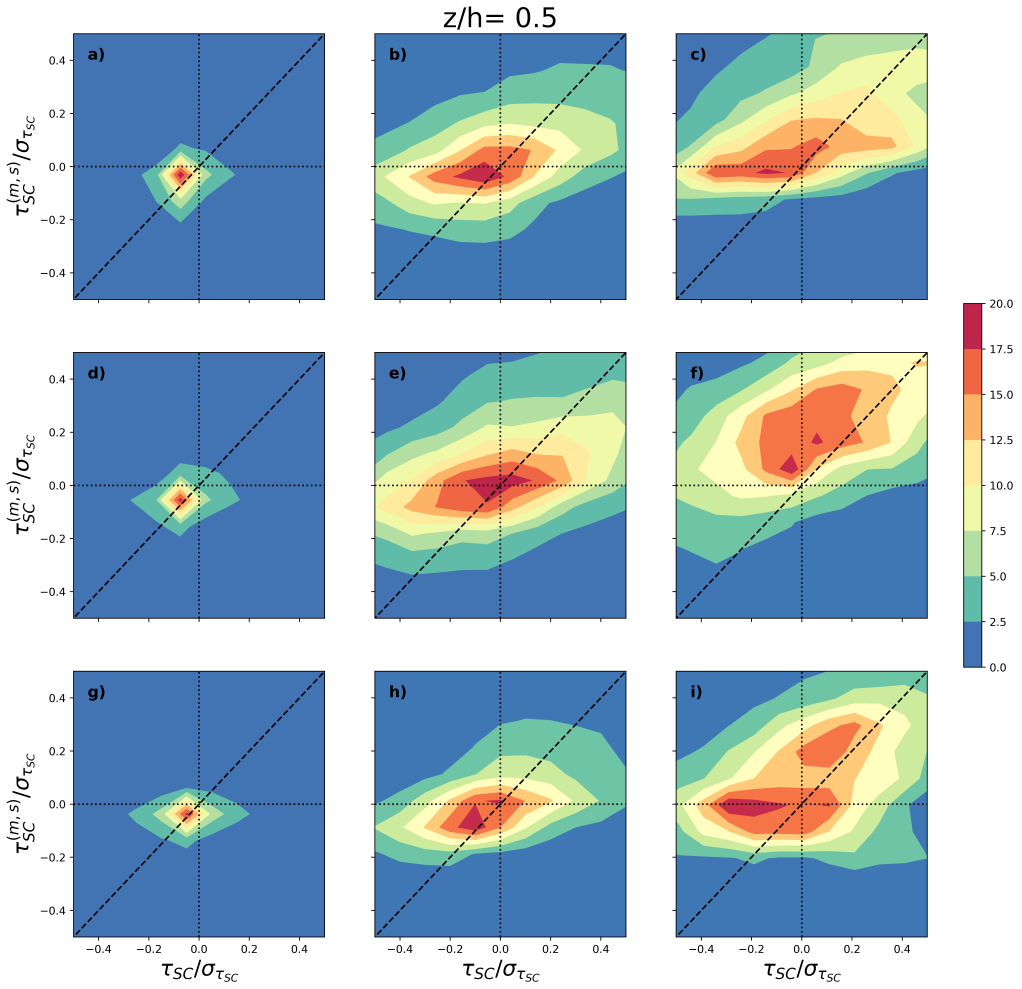

Figure 3.16: Joint probability density functions of the true SGS supersaturation and concentration covariance (τ_{SC}) and modeled supersaturation and concentration covariance for the similarity model ($\tau_{SC}^{m,s}$) normalized by the standard deviation of the true SGS term ($\sigma_{\tau_{SC}}$). All are plotted at one height (z/h=0.5) within the bulk of the flow. The injection rate increases from top to bottom: $\dot{n}$ = 1 (a-c), 10 (d-f), and 100 (g-i) $\mathrm{cm}^{-3}\,\mathrm{min}^{-1}$. The filter width increases from left to right: Δ/dx= 2 (a, d, g), 8 (b, e, h), and 16 (c, f, i).

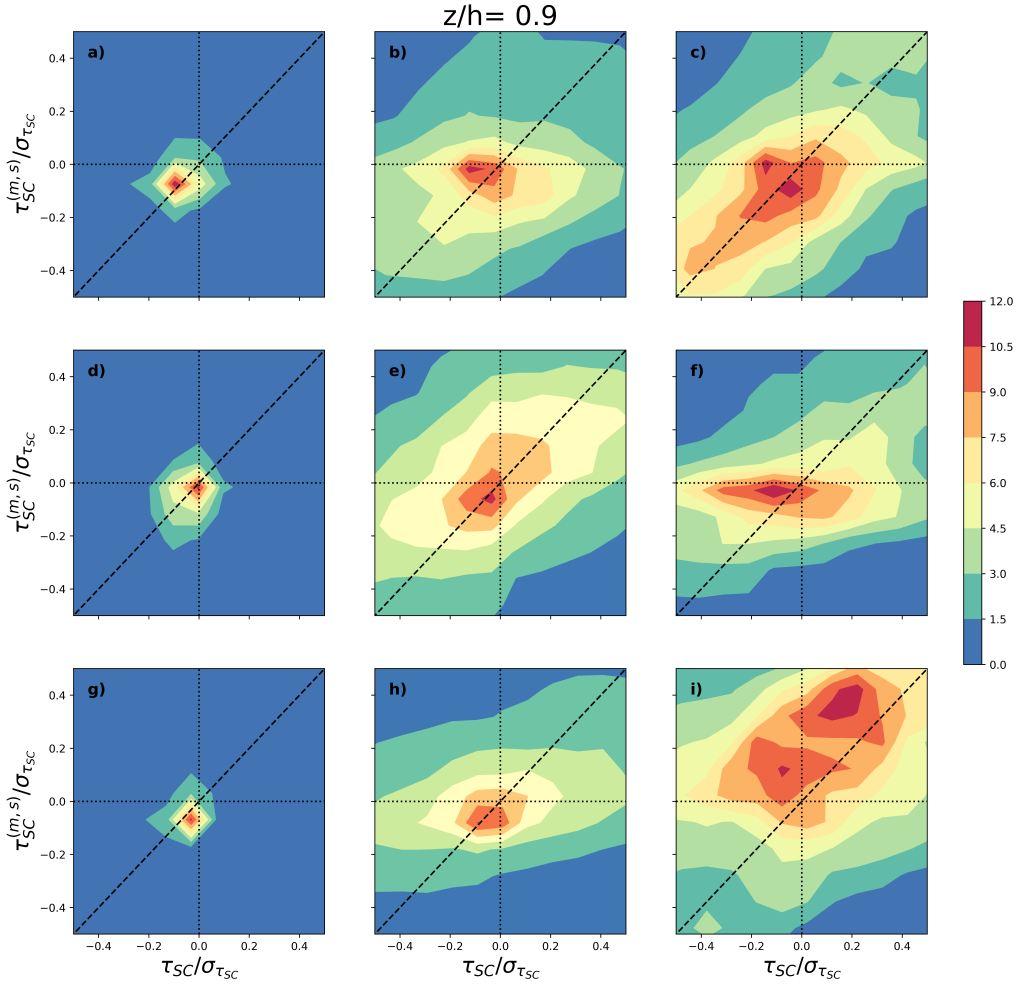

Figure 3.17: Joint probability density functions of the true SGS supersaturation and concentration covariance (τ_{SC}) and modeled supersaturation and concentration covariance for the similarity model ($\tau_{SC}^{m,s}$) normalized by the standard deviation of the true SGS term ($\sigma_{\tau_{SC}}$). All are plotted at one height (z/h=0.9) near the upper boundary layer. The injection rate increases from top to bottom: $\dot{n} = 1$ (a-c), 10 (d-f), and 100 (g-i) cm^{-3} min^{-1}. The filter width increases from left to right: Δ/dx= 2 (a, d, g), 8 (b, e, h), and 16 (c, f, i).

To assess the utility of the similarity model, the joint PDFs between the true (τ_{SC}) and modeled supersaturation and concentration covariance ($\tau_{SC}^{m,s}$) were performed for

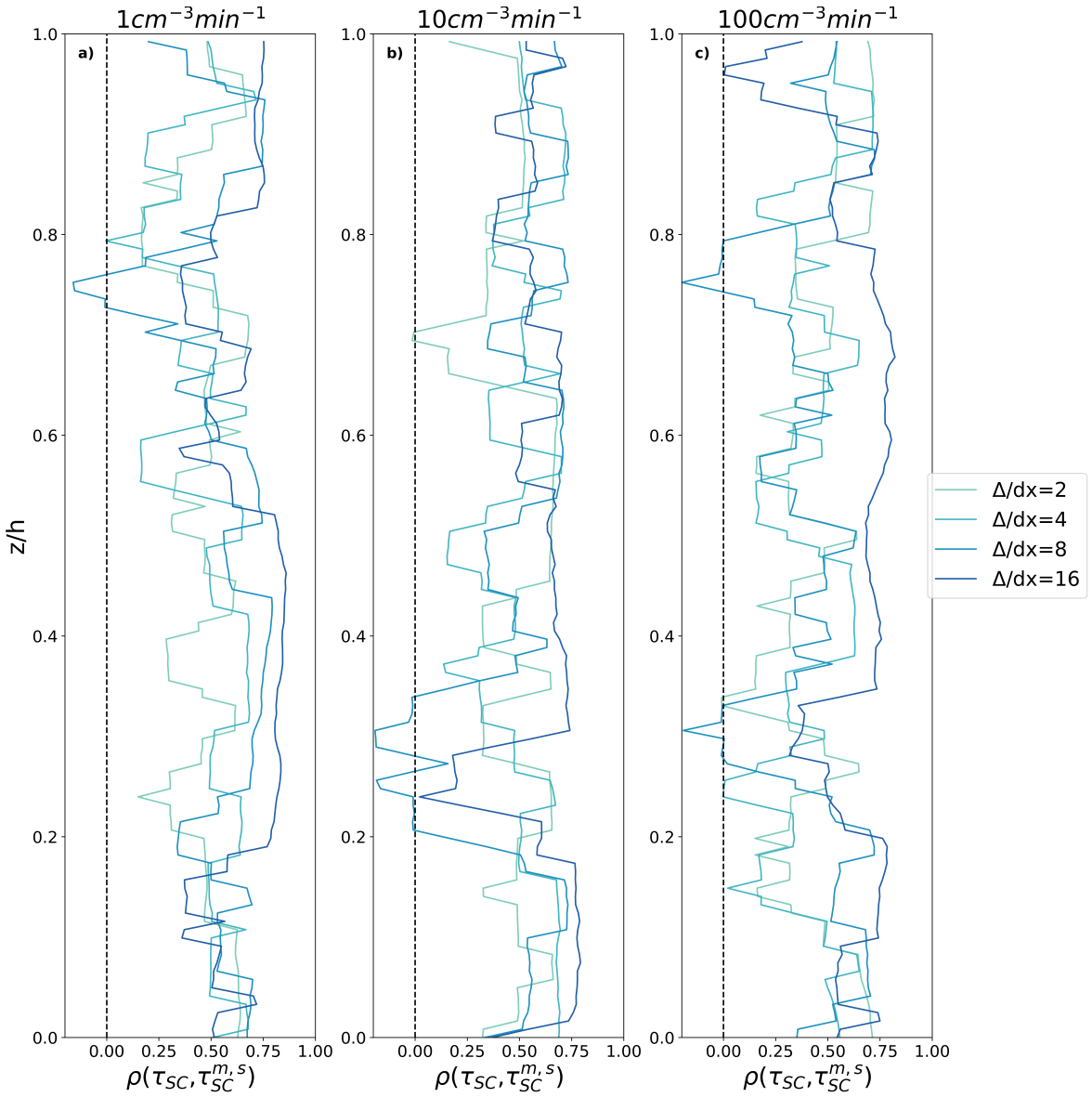

Figure 3.18: Correlation coefficients of the true SGS supersaturation and concentration covariance (τ_{SC}) and modeled supersaturation and concentration variance for the similarity model ($\tau_{SC}^{m,s}$) with height at varying filter widths and injection rates.

the same injection rates, filter widths, and heights as the gradient model (Figures 3.16 and 3.17). The joint PDFs did not indicate significant positive agreement between the similarity model and true SGS term particularly at the smallest filter width (Figures 3.16 and 3.17 (a), (d), and (g)). However, larger filter widths followed the one-to-one

line slightly better indicating better agreement the true and modeled SGS term. This was further assessed with the correlation coefficients.

Correlation coefficients between the true SGS and similarity-modeled supersaturation and concentration covariance were assessed between the varying injection rates and filter widths (Fig. 3.18). These were notable as they had considerable variability with height. Overall, the correlation coefficients range between $\rho \approx 0.3$–0.75. As such, the similarity model indicated relatively positive correlation between the true and modeled SGS covariance. It is worth noting that the largest filter width ($\Delta/dx = 16$) remained the most consistent with height as compared to the other filter widths for all injection rates. However, the variations with height may not indicate that this filter width is accurate for modeling the supersaturation and concentration covariance.

3.2.3 Discussion

When considering the supersaturation and concentration covariance, the gradient model did not show skill in predicting the SGS covariance. However, the similarity model indicated some skill in predicting the true SGS supersaturation and concentration covariance. The similarity model appeared to replicate the PDF of the true SGS supersaturation and concentration covariance and followed the one-to-one line in the joint PDFs indicating good agreement between the true and modeled SGS covariance at larger filter widths ($\Delta/dx = 8$ and 16). Despite correlation coefficients for the similarity model being significantly variable with height, they ranged between $\rho = 0.3 - 0.75$ which suggested there was relatively good agreement between the true and modeled SGS covariance. In contrast, the gradient model had a notably poor correlation between the true and modeled SGS covariance with correlation coefficients generally equal to $\rho = 0$. Despite relatively good correlations for the similarity model, further

investigation into alternative methods for modeling the supersaturation and concentration covariance may be warranted to better correlate the true SGS covariance to the modeled covariance.

3.3 Concentration Variance

The final term considered is the concentration covariance. As completed with the other SGS terms, the SGS fraction was calculated for three injection rates ($\dot{n}$ = 1, 10, and 100 $\mathrm{cm}^{-3}\,\mathrm{min}^{-1}$) and four filter widths (Δ/dx = 2, 4, 8, and 16, Fig. 3.19). Notable about this SGS fraction was that more than 90% of the true SGS concentration variance (τ_{CC}) occurred within the subgrid scales. While the smallest filter width ($\Delta/dx = 2$) indicated approximately 90% of the concentration occurred in the subgrid scales. However, larger filter widths suggested an SGS fraction between 95-100%. These results were significant as they indicate nearly all of the concentration covariance is within the subgrid scales and must be modeled by a subgrid-scale model. In addition, it is worth mentioning that the SGS fractions remained relatively constant with height. This is particularly notable as it suggests the concentration variance is not as influenced by the upper or lower boundary layers as the SGS terms including supersaturation.

To compare the gradient and similarity models with the true SGS concentration covariance, PDFs were plotted for the three injection rates analyzed previously and three filter widths (Δ/dx = 2, 8, and 16). In addition, Figure 3.20 was evaluated at z/h= 0.5, within the bulk of the flow, and Figure 3.21 was evaluated at z/h= 0.9, within the upper boundary layer. Each PDF was normalized by the standard deviation of the true SGS concentration variance ($\sigma_{\tau_{CC}}$). The PDFs were gamma-distributed for the smallest filter width (a), (d), (g) Δ/dx = 2 for all cases. The

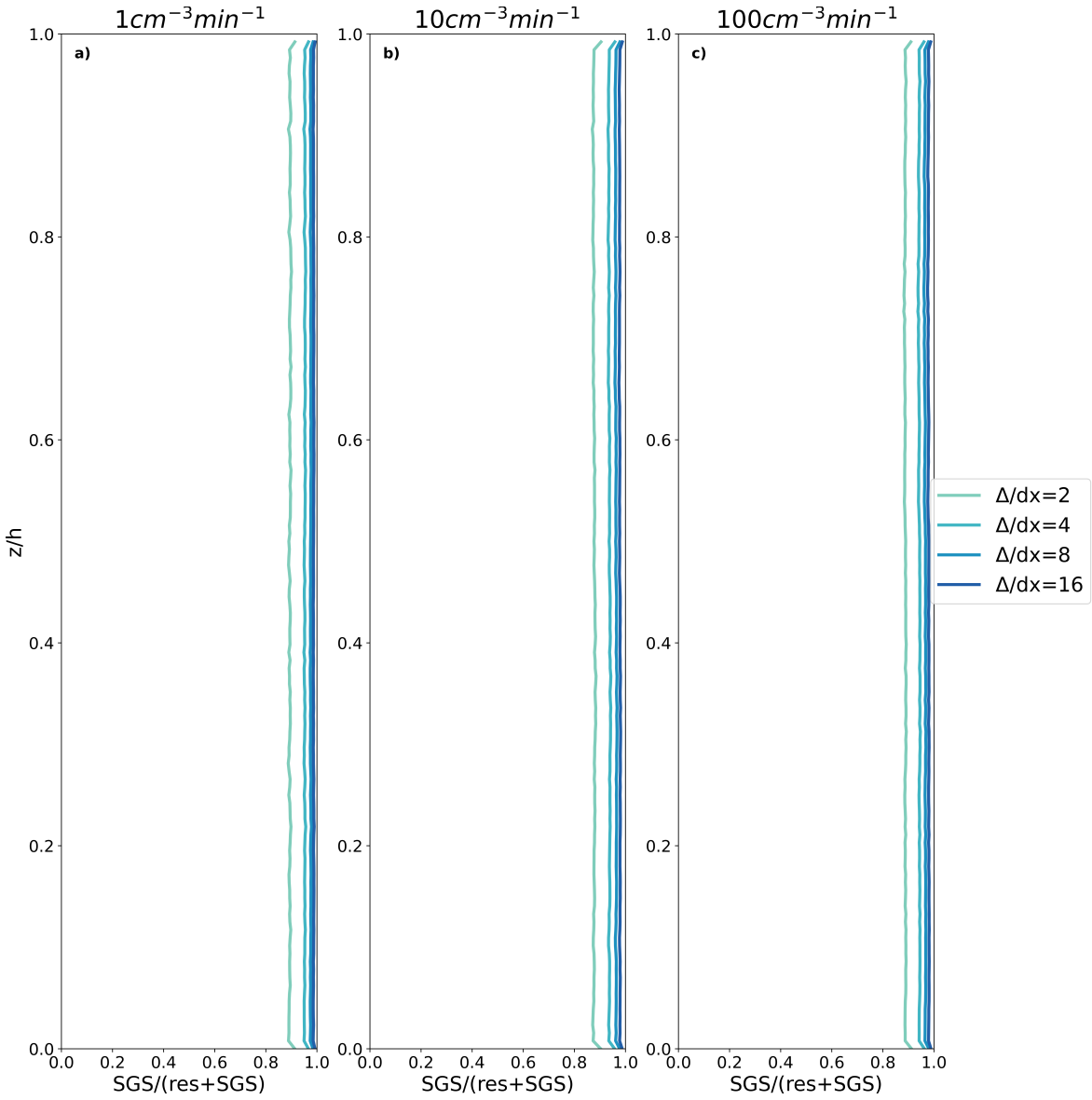

Figure 3.19: SGS fraction of the concentration variance with height at varying filter widths and injection rates.

larger filter widths transitioned to a nearly bimodal distribution, likely due to the large-scale circulation from Rayleigh-Bénard convection. While the similarity model showed some skill in representing these distributions, particularly at the lower filter widths (Δ/dx =2, and 8), the gradient model did not follow the PDFs of the true SGS concentration variance. This suggests decreased skill in the gradient model's ability

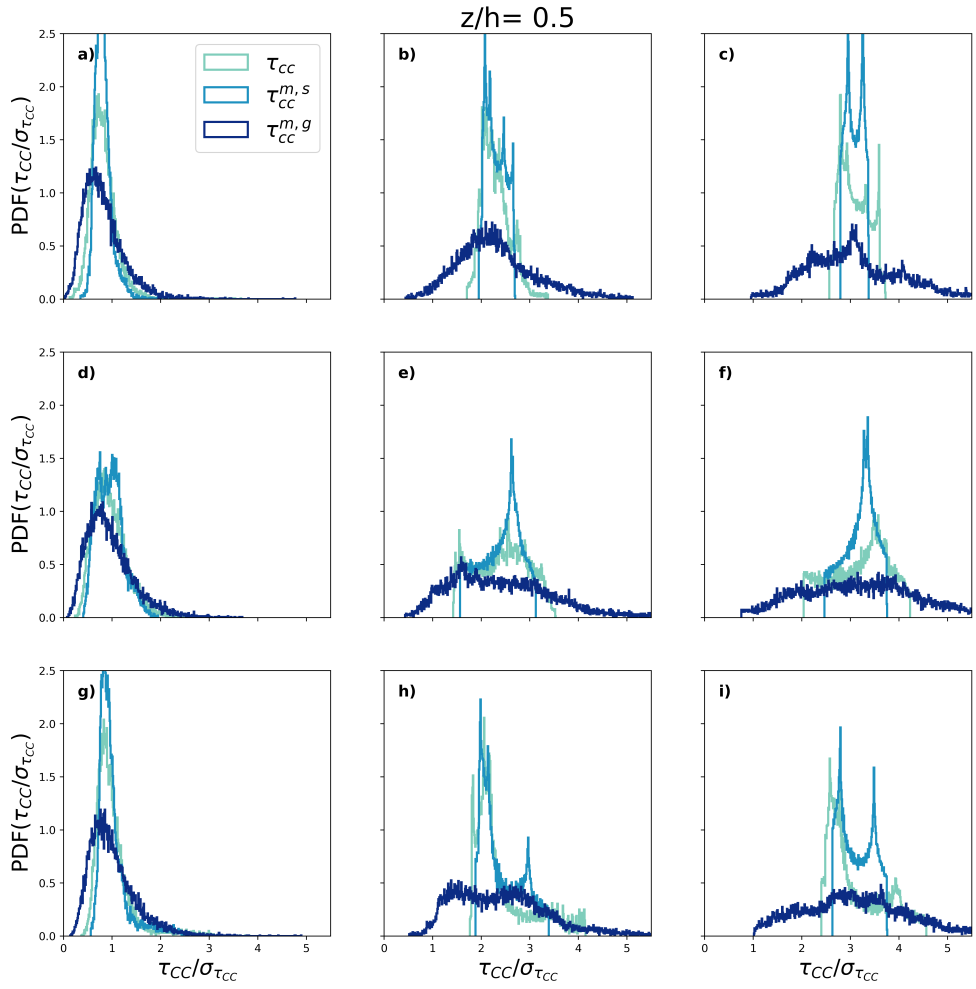

Figure 3.20: Probability density functions of the true SGS concentration variance (τ_{CC}) and modeled concentration variance for the similarity model ($\tau_{CC}^{m,s}$) and the gradient model ($\tau_{CC}^{m,g}$) normalized by the standard deviation of the true SGS term ($\sigma_{\tau_{CC}}$). All are plotted at one height (z/h=0.5) within the bulk of the flow. The injection rate increases from top to bottom: $\dot{n}$ = 1 (a-c), 10 (d-f), and 100 (g-i) $\mathrm{cm}^{-3}\,\mathrm{min}^{-1}$. The filter width increases from left to right: Δ/dx= 2 (a, d, g), 8 (b, e, h), and 16 (c, f, i).

to represent this SGS variance. These hypotheses will be quantified in the following sections to better qualitatively and quantitatively assess each model's accuracy.

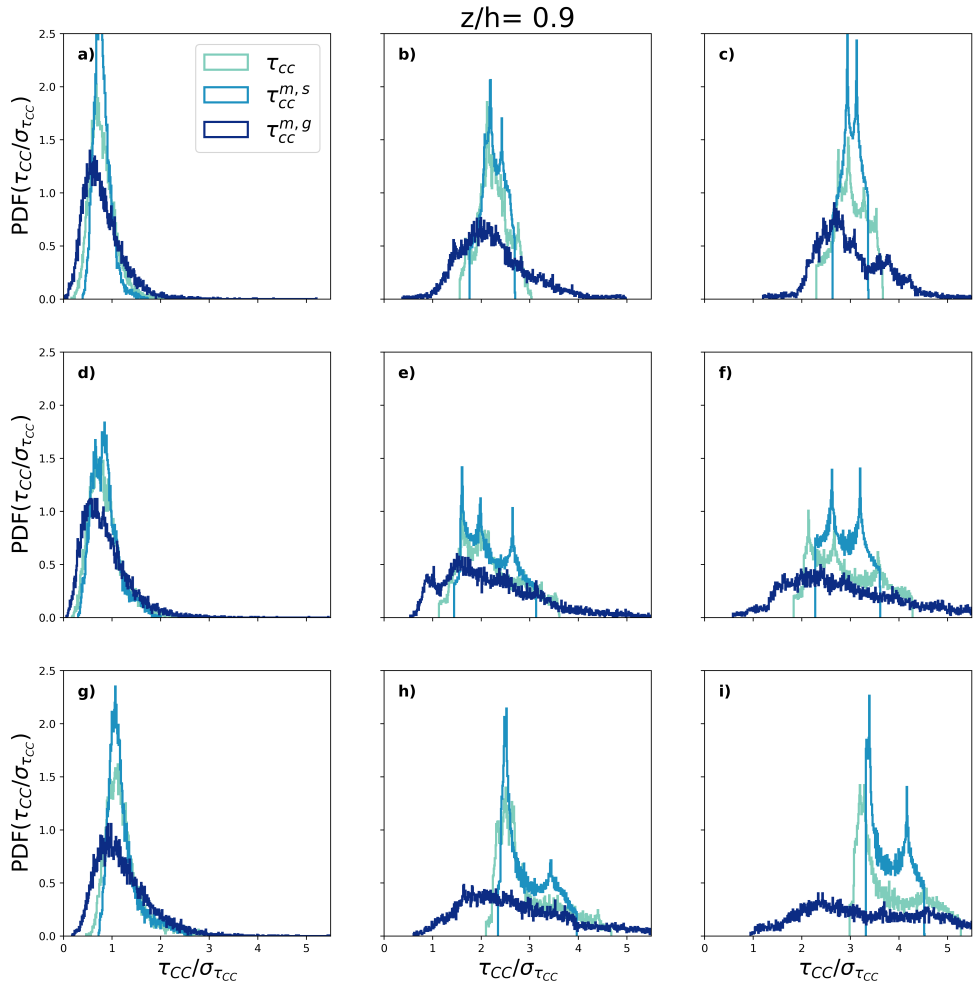

Figure 3.21: Probability density functions of the true SGS concentration variance (τ_{CC}) and modeled concentration variance for the similarity model ($\tau_{CC}^{m,s}$) and the gradient model ($\tau_{CC}^{m,g}$) normalized by the standard deviation of the true SGS term ($\sigma_{\tau_{CC}}$). All are plotted at one height (z/h=0.9) near the upper boundary layer. The injection rate increases from top to bottom: $\dot{n}$ = 1 (a-c), 10 (d-f), and 100 (g-i) cm^{-3} min^{-1}. The filter width increases from left to right: Δ/dx= 2 (a, d, g), 8 (b, e, h), and 16 (c, f, i).

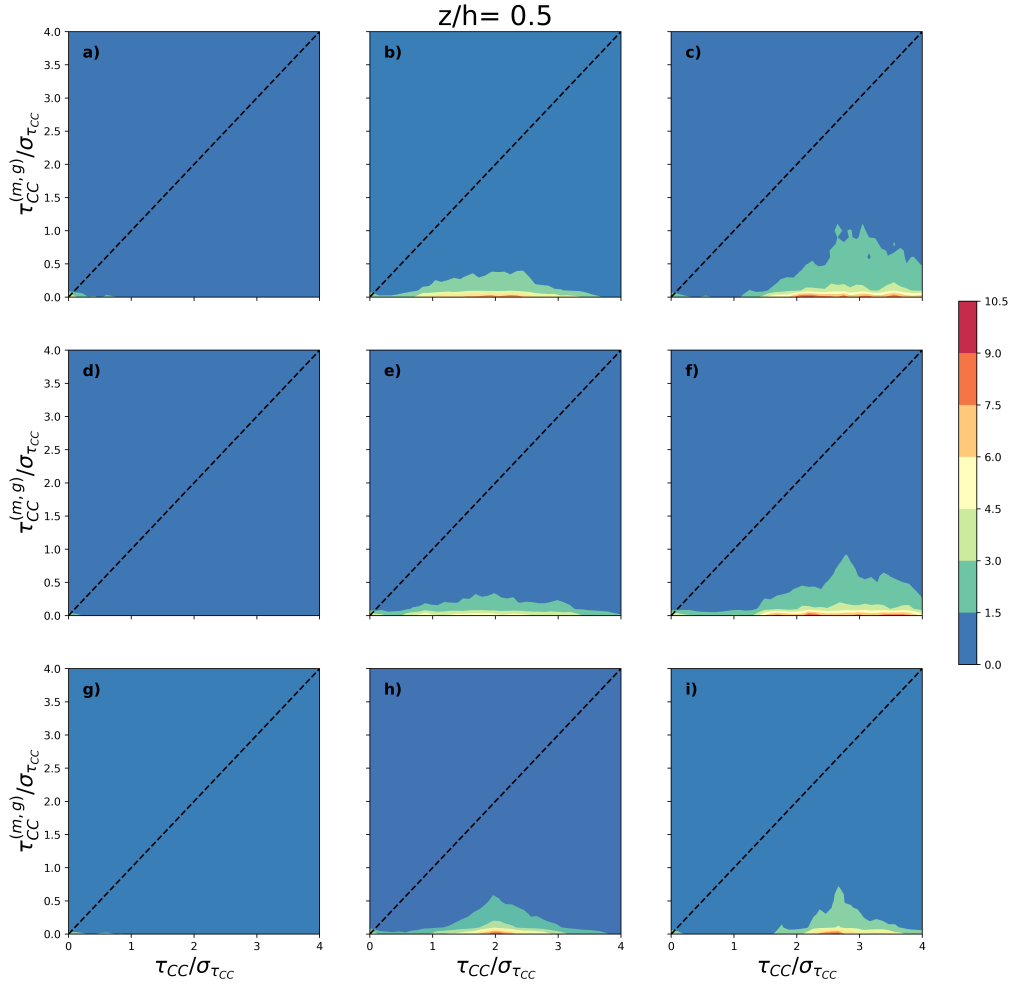

Figure 3.22: Joint probability density functions of the true SGS concentration variance (τ_{CC}) and modeled supersaturation variance for the gradient model ($\tau_{CC}^{m,g}$) normalized by the standard deviation of the true SGS term ($\sigma_{\tau_{CC}}$). All are plotted at one height (z/h=0.5) within the bulk of the flow. The injection rate increases from top to bottom: $\dot{n}$ = 1 (a-c), 10 (d-f), and 100 (g-i) cm^{-3} min^{-1}. The filter width increases from left to right: Δ/dx= 2 (a, d, g), 8 (b, e, h), and 16 (c, f, i).

3.3.1 Gradient Model

To assess the ability of the gradient model to represent the true SGS concentration covariance (τ_{CC}), joint PDFs were plotted for the same injection rates, filter widths,

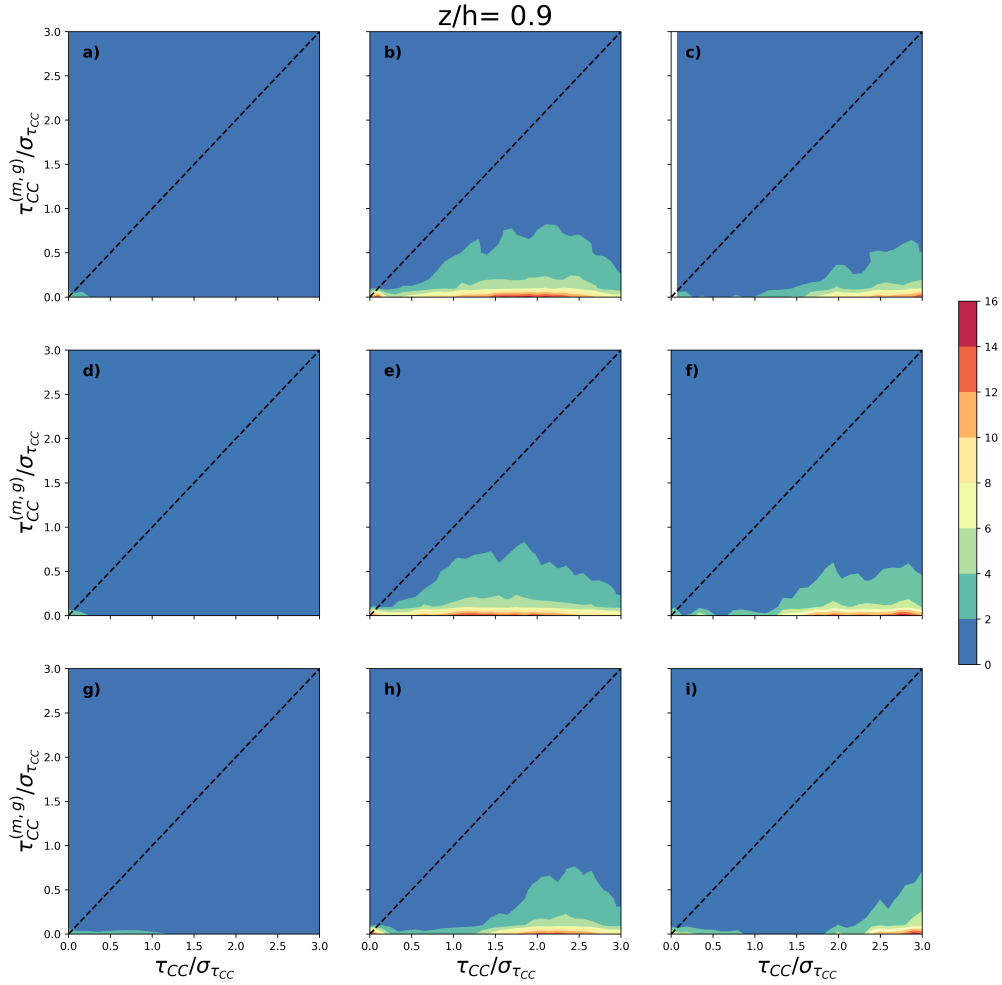

Figure 3.23: Joint probability density functions of the true SGS concentration variance (τ_{CC}) and modeled supersaturation variance for the gradient model ($\tau_{CC}^{m,g}$) normalized by the standard deviation of the true SGS term ($\sigma_{\tau_{CC}}$). All are plotted at one height (z/h=0.9) near the upper boundary layer. The injection rate increases from top to bottom: $\dot{n}$ = 1 (a-c), 10 (d-f), and 100 (g-i) $\mathrm{cm}^{-3}\,\mathrm{min}^{-1}$. The filter width increases from left to right: Δ/dx= 2 (a, d, g), 8 (b, e, h), and 16 (c, f, i).

and heights described for the PDFs discussed previously (Figures 3.22 and 3.23). It is first important to note that the joint PDFs for the smallest filter widths (Δ/dx = 2) had small magnitudes. This was likely due to statistical convergence limitations

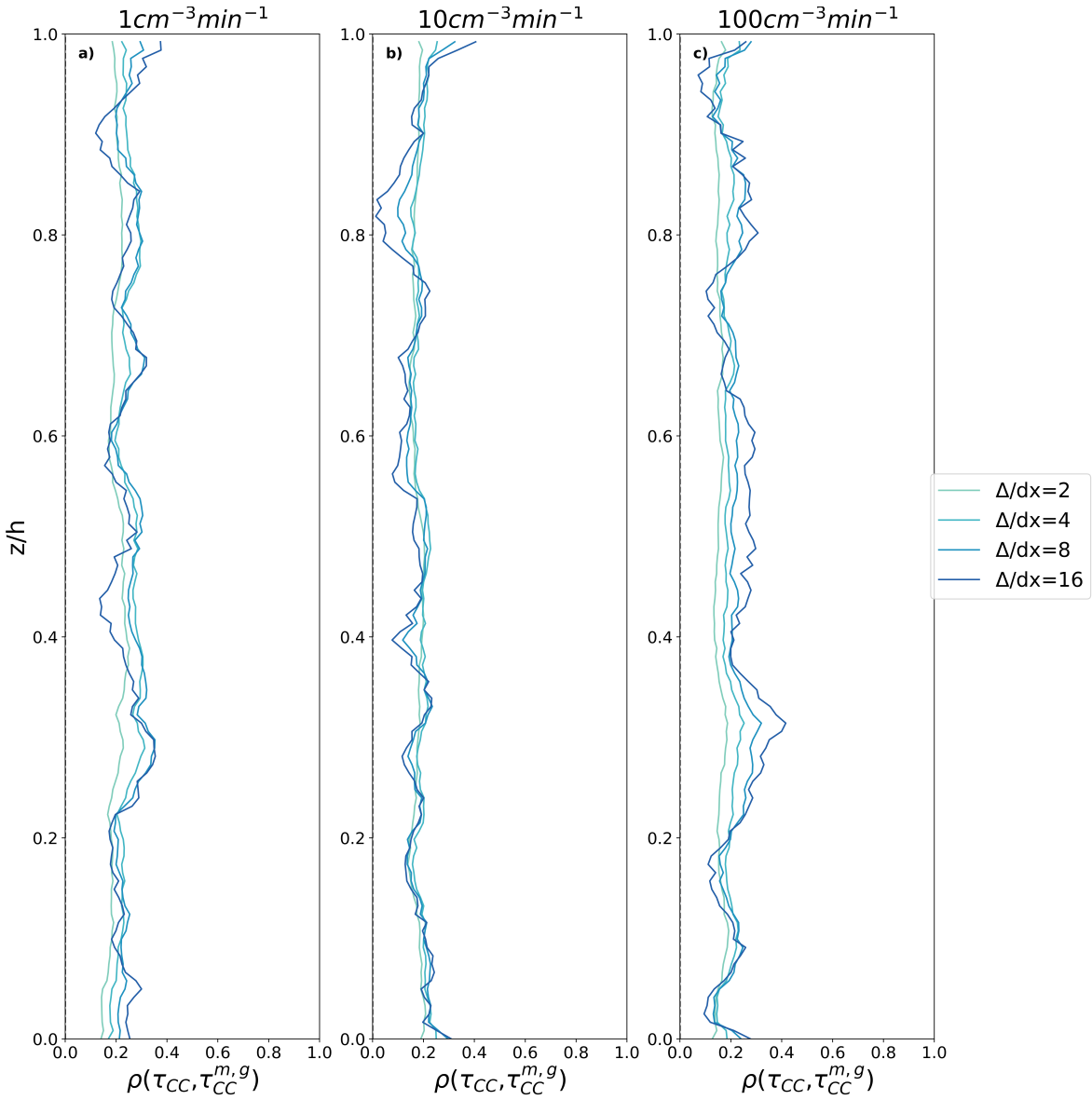

Figure 3.24: Correlation coefficients of the true SGS concentration variance (τ_{CC}) and modeled supersaturation and concentration variance for the gradient model ($\tau_{CC}^{m,g}$) with height at varying filter widths and injection rates.

as there are few particles at each grid cell. However, to remain consistent with past variance and covariance terms, these filter widths and bin spacing were selected for comparison. Regardless, the joint PDFs did not closely follow the one-to-one line that indicates good agreement between the gradient-modeled SGS concentration variance

($\tau_{CC}^{m,c}$) and the true SGS concentration variance. This was true across all cases, and all followed similar trends independent of injection rate, filter width, or height.

Relatively poor agreement between the true SGS concentration covariance and SGS concentration covariance modeled by the gradient model was further supported by the correlation coefficients plotted in Figure 3.24. Here, the gradient model had low correlation coefficients of approximately ρ =0.2 for all injection rates and filter widths. It may be worthwhile to consider increasing filter width had a notable increase in the variability of correlation coefficient values with height. However, it did not appear that any filter width had particularly better or worse correlation coefficients that would result in a recommendation for further use in developing a subgrid-scale model.

3.3.2 Similarity Model

The injection rates, filter widths, and heights investigated for the PDFs and joint PDFs for the gradient model were also assessed between the true SGS concentration variance (τ_{CC}) and the modeled SGS concentration variance with the similarity model ($\tau_{CC}^{m,s}$, Figures 3.25 and 3.26). As was observed with the gradient model, there were few contours for the joint PDFs for the smallest filter width (Fig. 3.25 (a), (d), and (g)), likely due to a small number of particles at each grid point which became filtered out at small filter widths. However, the data observed seemed to follow the one-to-one line indicating positive agreement between the true and modeled SGS variance. Further, this trend was observed for the remainder of the injection rates, filter widths, and heights. The joint PDFs appeared to follow the one-to-one line closely, suggesting the similarity model likely has good skill in representing the concentration variance term.

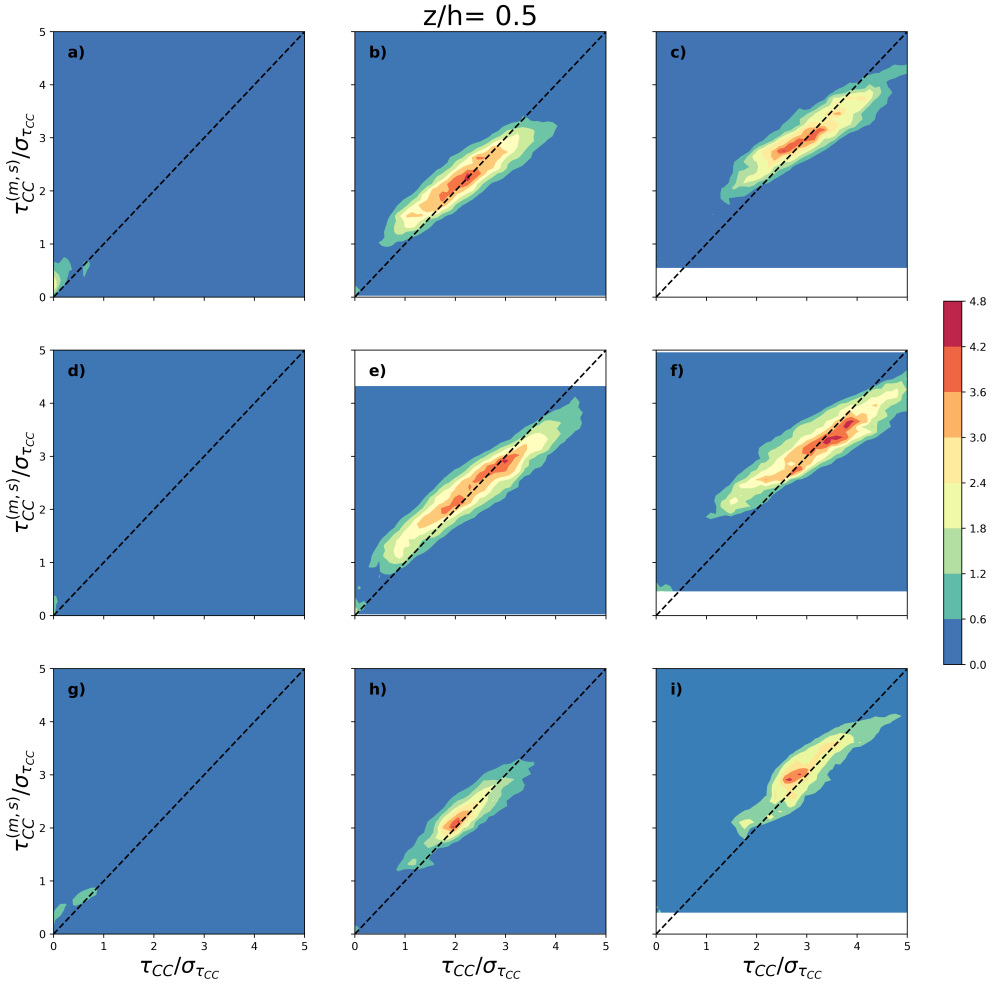

Figure 3.25: Joint probability density functions of the true SGS concentration variance (τ_{CC}) and modeled supersaturation variance for the similarity model ($\tau_{CC}^{m,s}$) normalized by the standard deviation of the true SGS term ($\sigma_{\tau_{CC}}$). All are plotted at one height (z/h=0.5) within the bulk of the flow. The injection rate increases from top to bottom: $\dot{n}$ = 1 (a-c), 10 (d-f), and 100 (g-i) $\mathrm{cm}^{-3}\,\mathrm{min}^{-1}$. The filter width increases from left to right: Δ/dx= 2 (a, d, g), 8 (b, e, h), and 16 (c, f, i).

The correlation coefficients for each injection rate and filter width with height also supported positive agreement between the true SGS concentration variance and the

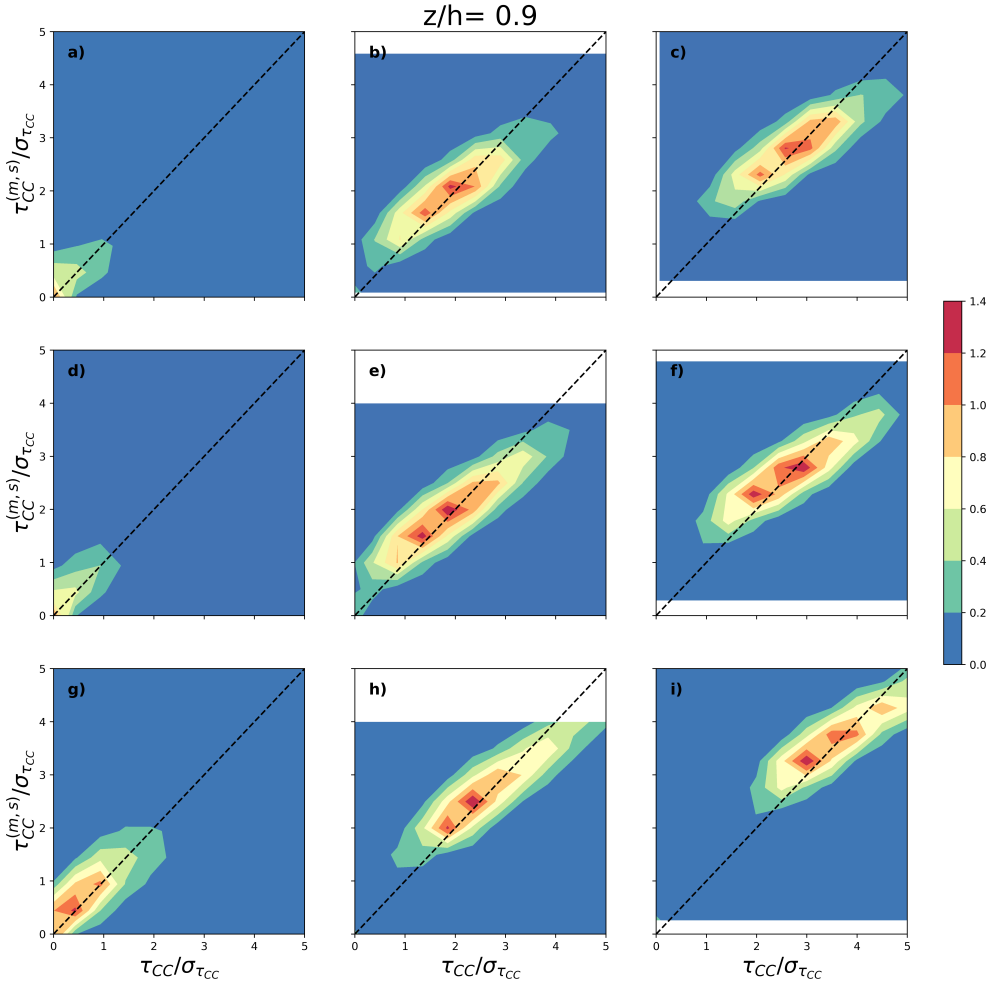

Figure 3.26: Joint probability density functions of the true SGS concentration variance (τ_{CC}) and modeled supersaturation variance for the similarity model ($\tau_{CC}^{m,s}$) normalized by the standard deviation of the true SGS term ($\sigma_{\tau_{CC}}$). All are plotted at one height (z/h=0.9) near the upper boundary layer. The injection rate increases from top to bottom: $\dot{n}$ = 1 (a-c), 10 (d-f), and 100 (g-i) cm^{-3} min^{-1}. The filter width increases from left to right: Δ/dx= 2 (a, d, g), 8 (b, e, h), and 16 (c, f, i).

similarity model values of concentration variance (Fig. 3.27). All cases observed correlation coefficients above $\rho = 0.8$ indicating the similarity model does have skill in representing the true SGS concentration variance. A considerable result also indicated

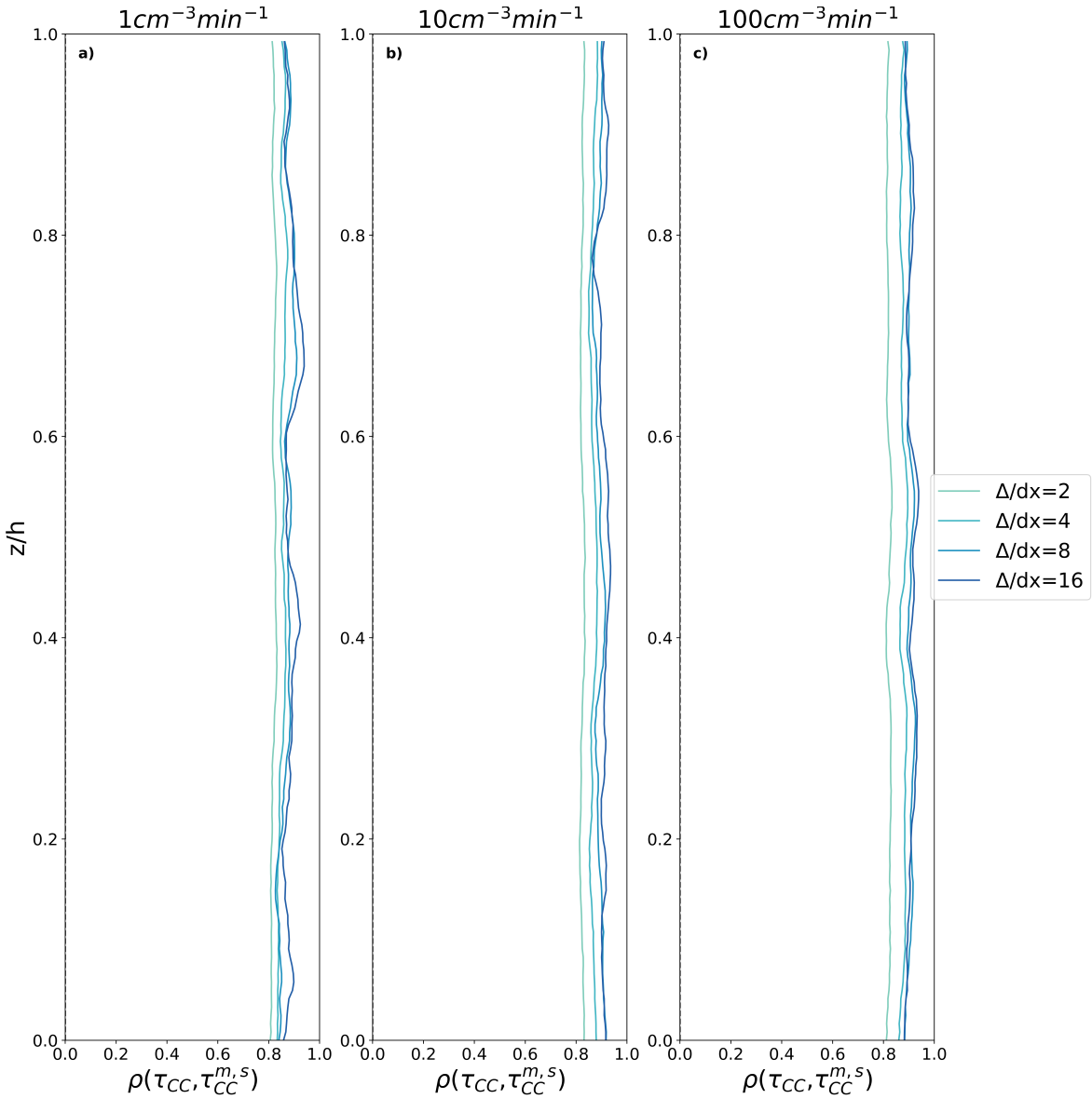

Figure 3.27: Correlation coefficients of the true SGS concentration variance (τ_{CC}) and modeled supersaturation and concentration variance for the similarity model ($\tau_{CC}^{m,s}$) with height at varying filter widths and injection rates.

that the correlation coefficients improved with increasing filter width. This is a significant result as it supports the use of a larger filter width to model the SGS concentration variance which would improve computational efficiency than if a smaller filter width was selected.

3.3.3 Discussion

When the utility of the gradient and similarity models were compared to the true SGS concentration variance, the similarity model had better skill in capturing the trends in the true SGS variance. This was supported by all methods of analysis where the PDFs did not replicate the true SGS concentration variance well, the joint PDFs did not closely follow the one-to-one line, and correlation coefficients were low. However, the similarity model did show skill for each case to accurately represent the true SGS concentration variance. Overall, the PDFs followed the trend of the true SGS variance, the joint PDFs followed the one-to-one line closely for all cases, and the correlation coefficients were generally greater than $\rho = 0.8$. Further, it appeared that larger filter widths may improve the accuracy of the modeled SGS variance. This was particularly noted in the correlation coefficients for the similarity model which increased in magnitude with increasing filter width. As such, it is likely that the similarity model would be best suited for further development into a subgrid-scale model.

3.4 Relevance to Previous Studies

Few past studies have investigated ways to model all SGS terms considered in this work. However, Salesky et al. (2024) assessed the SGS scalar variance with data from the Pi Chamber. This study also compared the use of both the similarity and gradient models for representing the SGS supersaturation variance. The results in this thesis followed closely to those outlined in Salesky et al. (2024). The gradient model was found to have fairly poor skill in representing the SGS supersaturation variance with correlation coefficients of $\rho \approx 0.2$, comparable to the $\rho \approx 0.1 - 0.4$ observed in this study. Salesky et al. (2024) also found that the similarity model more accurately represented the SGS supersaturation variance with correlation coefficients of $\rho \approx 0.8$

which aligned with correlation coefficients between $\rho = 0.75 - 0.9$ found in this study. Therefore, there is a strong indication that the similarity model is the best candidate for future subgrid-scale models of supersaturation variance.

Despite the supersaturation and concentration covariance and concentration variance not being assessed in Salesky et al. (2024), Liu et al. (1994) provides support for the use of the similarity model to represent the supersaturation and concentration covariance. While Liu et al. (1994) focused on modeling the SGS stress tensor, correlation coefficients between the true SGS stress tensor and filtered strain rate tensor were less than $\rho \approx 0.2$ for the Smagorinsky model which is readily used in LES models. This is lower than the $\rho = 0.25 - 0.75$ observed by the similarity model in this study. As a result, an argument could be made for the similarity model to represent the SGS supersaturation and concentration covariance. Finally, while studies evaluating concentration variance were lacking, high correlation coefficients ($\rho = 0.8 - 0.9$) for the similarity model suggest considerable agreement supporting its use for an SGS model to implement into LES. While the gradient model indicated less skill with correlation coefficients near $\rho = 0.2$, low correlation coefficients are often used for SGS models of momentum (Liu et al., 1994). This suggests the gradient model may be warranted to represent the concentration covariance. Overall, it is recommended that the similarity model be used to represent the SGS terms evaluated in this analysis (τ_{SS}, τ_{SC}, and τ_{CC}).

Chapter 4

Summary and Conclusions

Clouds have a significant impact on Earth's weather and climate systems but remain poorly understood. Studies have suggested that turbulence can induce supersaturation fluctuations which result in broader droplet size distributions (Vaillancourt and Yau, 2000; Grabowski and Wang, 2013). As a result, this could improve the collision efficiency of droplets supporting better efficiency of precipitation development. However, these processes occur on small scales (micrometers to millimeters) making them difficult to study.

Recent studies have investigated the role turbulence plays in cloud microphysics using laboratory facilities such as the Pi Chamber at Michigan Technological University, direct numerical simulations, and large eddy simulations. Results from these studies observed possible preferential droplet growth zones where supersaturation fluctuations were observed (Prabhakaran et al., 2020; Shawon et al., 2021; Anderson et al., 2021). Further, they concluded that droplet history plays a significant role in understanding a particle's potential to activate in the future (Thomas et al., 2020; MacMillan et al., 2022). These small-scale details are important particularly when considering studies involving large eddy simulations. Large eddy simulations are useful due to their computational efficiency. They obtain this by fully resolving the large scales of motion and modeling the smallest scales. While some studies have investigated modeling the stress tensor and scalar flux vector, terms related to interactions between turbulence

and cloud microphysics have received little attention. Modeling these small-scale interactions with accuracy is significantly important in understanding cloud microphysics processes and their broader impacts. Currently, no subgrid scale terms represent some of these processes; it is these terms that were investigated.

This study examined three subgrid scale quantities: supersaturation variance (τ_{SS}), supersaturation and concentration covariance (τ_{SC}), and concentration variance (τ_{CC}). The supersaturation variance appears in Lagrangian microphysics where a stochastic term contains both the resolved and subgrid-scale supersaturation variance. While the resolved supersaturation variance can be derived from explicitly resolved terms, the subgrid-scale supersaturation variance must be modeled. However, the development and testing of accurate models for the SGS supersaturation variance has received little attention to date. Similarly, supersaturation and concentration covariance and concentration variance are terms that arise when the evolution equation for droplet size distribution (eq. 1.1) is filtered and applied in an Eulerian framework. The subgrid-scale covariance and variance both have resolved and modeled components in LES. While the resolved components are explicitly calculated in LES, subgrid scale models do not currently exist for the modeled components. It was the goal of this study to identify potential subgrid-scale models to be implemented into LES.

To study the SGS variance and covariance terms of interest, this project evaluated an ensemble of direct numerical simulations similar to the Pi Chamber. These simulations induced Rayleigh-Bénard convection with Rayleigh numbers of 7.9×10^6. Five cases were tested with varying injection rates: 1, 3, 10, 30, and 100 $\mathrm{cm}^{-3}\,\mathrm{min}^{-1}$. While supersaturation in the DNS was higher than in the Pi Chamber and the Rayleigh number was lower than achievable in the Pi Chamber, the results are still valid as this was a turbulent flow with particles that could activate and form cloud condensation nuclei. Despite the limitations, a benefit of these methods was the ability to gather

information on Lagrangian particles. As a result, particle size information could be investigated as it correlated to the background flow.

From the DNS data, both the true SGS terms of interest (τ_{SS}, τ_{SC}, and τ_{CC}) and candidate models could be calculated. Then, the true subgrid scale quantities were compared to two candidate models: the gradient model and the scale-similarity model. The accuracy of each model was evaluated with several statistical methods including probability density functions, joint probability density functions, and correlation coefficients. Each model was compared across the subgrid scale terms of interest for varying injection rates, filter widths, and heights in the domain. Results indicated that the gradient model did not perform exceptionally well in any case with correlation coefficients between $\rho \approx 0 - 0.4$. However, the similarity model did show skill in predicting the true subgrid scale terms with correlation coefficients ranging between $\rho \approx 0.3 - 0.9$. This was particularly true for the supersaturation and concentration variances. These results followed closely with recent work published by Salesky et al. (2024). While neither the gradient model nor the similarity model performed exceptionally well for the supersaturation and concentration covariance, the similarity model performed significantly better ($\rho = 0.3 - 0.75$) than the gradient model ($\rho = 0$). Further, results were similar to other subgrid-scale models currently in practice for the SGS stress tensor which has correlation coefficients of $\rho \approx 0.2$ (Liu et al., 1994). As such, it was recommended that the similarity model be used to represent the subgrid-scale terms evaluated in this study in future subgrid-scale models.

It is important to note that this study contained limitations primarily related to the maximum Rayleigh numbers achievable. In particular, the maximum number of particles able to be injected into the simulation was another limitation. As a result, comparisons of concentrations between particles of different radii could not be conducted due to a lack of statistical convergence. Future work should expand the Rayleigh numbers

simulated to remain more consistent with the Pi Chamber while also increasing the number of particles within the flow. Further, unrealistic supersaturation values should be a consideration when evaluating these results. While it was not hypothesized that these errors would have significant influences on the quality of the results, the exact implications of the results are not fully understood. In particular, the influence that mean supersaturation has on droplet activation is uncertain and should be investigated further. Finally, future work should implement these results into a subgrid-scale model in LES. From there, the performance of the model should be assessed with a posteriori testing to evaluate accuracy in representing these terms.

Reference List

Anderson, J. C., S. Thomas, P. Prabhakaran, R. A. Shaw, and W. Cantrell, 2021: Effects of the large-scale circulation on temperature and water vapor distributions in the π chamber. *Atmospheric Measurement Techniques*, **14 (8)**, 5473–5485, https://doi.org/10.5194/amt-14-5473-2021, URL https://amt.copernicus.org/articles/14/5473/2021/.

Beard, K. V., and H. T. Ochs, 1993: Warm-rain initiation: An overview of microphysical mechanisms. *Journal of Applied Meteorology and Climatology*, **32 (4)**, 608 – 625, https://doi.org/https://doi.org/10.1175/1520-0450(1993)032⟨0608:WRIAOO⟩2.0.CO;2, URL https://journals.ametsoc.org/view/journals/apme/32/4/1520-0450_1993_032_0608_wriaoo_2_0_co_2.xml.

Chang, K., and Coauthors, 2016: A laboratory facility to study gas–aerosol–cloud interactions in a turbulent environment: The π chamber. *Bulletin of the American Meteorological Society*, **97 (12)**, 2343 – 2358, https://doi.org/https://doi.org/10.1175/BAMS-D-15-00203.1, URL https://journals.ametsoc.org/view/journals/bams/97/12/bams-d-15-00203.1.xml.

Chumakov, S. G., 2008: A priori study of subgrid-scale flux of a passive scalar in isotropic homogeneous turbulence. *Phys. Rev. E*, **78**, 036 313, https://doi.org/10.1103/PhysRevE.78.036313, URL https://link.aps.org/doi/10.1103/PhysRevE.78.036313.

Devenish, B. J., and Coauthors, 2012: Droplet growth in warm turbulent clouds. *Quarterly Journal of the Royal Meteorological Society*, **138 (667)**, 1401–1429, https://doi.org/https://doi.org/10.1002/qj.1897, URL https://rmets.onlinelibrary.wiley.com/doi/abs/10.1002/qj.1897.

Grabowski, W. W., 2020: Comparison of Eulerian bin and Lagrangian particle-based schemes in simulations of Pi chamber dynamics and microphysics. *Journal of the Atmospheric Sciences*, **77 (3)**, 1151–1165.

Grabowski, W. W., and G. C. Abade, 2017: Broadening of cloud droplet spectra through eddy hopping: Turbulent adiabatic parcel simulations. *Journal of the Atmospheric Sciences*, **74 (5)**, 1485 – 1493, https://doi.org/https://doi.org/10.1175/JAS-D-17-0043.1, URL https://journals.ametsoc.org/view/journals/atsc/74/5/jas-d-17-0043.1.xml.

Grabowski, W. W., and L.-P. Wang, 2013: Growth of cloud droplets in a turbulent environment. *Annual Review of Fluid Mechanics*, **45 (1)**, 293–324, https://doi.org/10.1146/annurev-fluid-011212-140750, URL https://doi.org/10.1146/annurev-fluid-011212-140750.

Higgins, C. W., C. Meneveau, and M. B. Parlange, 2007: The effect of filter dimension on the subgrid-scale stress, heat flux, and tensor alignments in the atmospheric surface layer. *Journal of Atmospheric and Oceanic Technology*, **24 (3)**, 360–375.

Hoffmann, F., and G. Feingold, 2019: Entrainment and mixing in stratocumulus: Effects of a new explicit subgrid-scale scheme for large-eddy simulations with particle-based microphysics. *Journal of the Atmospheric Sciences*, **76 (7)**, 1955 – 1973, https://doi.org/10.1175/JAS-D-18-0318.1, URL https://journals.ametsoc.org/view/journals/atsc/76/7/jas-d-18-0318.1.xml.

Hu, A. Z., and A. L. Igel, 2023: A bin and a bulk microphysics scheme can be more alike than two bin schemes. *Journal of Advances in Modeling Earth Systems*, **15 (3)**, https://doi.org/https://doi.org/10.1029/2022MS003303, URL https://agupubs.onlinelibrary.wiley.com/doi/abs/10.1029/2022MS003303, https://agupubs.onlinelibrary.wiley.com/doi/pdf/10.1029/2022MS003303.

Khain, A. P., and Coauthors, 2015: Representation of microphysical processes in cloud-resolving models: Spectral (bin) microphysics versus bulk parameterization. *Reviews of Geophysics*, **53 (2)**, 247–322, https://doi.org/https://doi.org/10.1002/2014RG000468.

Kumar, B., P. Götzfried, N. Suresh, J. Schumacher, and R. A. Shaw, 2018: Scale dependence of cloud microphysical response to turbulent entrainment and mixing. *Journal of Advances in Modeling Earth Systems*, **10 (11)**, 2777–2785, https://doi.org/https://doi.org/10.1029/2018MS001487, URL https://agupubs.onlinelibrary.wiley.com/doi/abs/10.1029/2018MS001487.

Kumar, B., J. Schumacher, and R. A. Shaw, 2013: Cloud microphysical effects of turbulent mixing and entrainment. *Theoretical and Computational Fluid Dynamics*, **27 (3)**, 361–376, https://doi.org/10.1007/s00162-012-0272-z, URL https://doi.org/10.1007/s00162-012-0272-z.

Kumar, B., J. Schumacher, and R. A. Shaw, 2014: Lagrangian mixing dynamics at the cloudy–clear air interface. *Journal of the Atmospheric Sciences*, **71 (7)**, 2564 – 2580, https://doi.org/https://doi.org/10.1175/JAS-D-13-0294.1, URL https://journals.ametsoc.org/view/journals/atsc/71/7/jas-d-13-0294.1.xml.

Lanotte, A. S., A. Seminara, and F. Toschi, 2009: Cloud droplet growth by condensation in homogeneous isotropic turbulence. *Journal of the Atmospheric Sciences*, **66 (6)**, 1685 – 1697, https://doi.org/https://doi.org/10.1175/2008JAS2864.1, URL https://journals.ametsoc.org/view/journals/atsc/66/6/2008jas2864.1.xml.

Liu, S., C. Meneveau, and J. Katz, 1994: On the properties of similarity subgrid-scale models as deduced from measurements in a turbulent jet. *Journal of Fluid Mechanics*, **275**, 83–119, https://doi.org/10.1017/S0022112094002296.

MacMillan, T., R. A. Shaw, W. H. Cantrell, and D. H. Richter, 2022: Direct numerical simulation of turbulence and microphysics in the Pi chamber. *Phys. Rev. Fluids*, **7**, 020 501, https://doi.org/10.1103/PhysRevFluids.7.020501, URL https://link.aps.org/doi/10.1103/PhysRevFluids.7.020501.

Morrison, H., M. Witte, G. H. Bryan, J. Y. Harrington, and Z. J. Lebo, 2018: Broadening of modeled cloud droplet spectra using bin microphysics in an Eulerian spatial domain. *Journal of the Atmospheric Sciences*, **75 (11)**, 4005 – 4030, https://doi.org/https://doi.org/10.1175/JAS-D-18-0055.1, URL https://journals.ametsoc.org/view/journals/atsc/75/11/jas-d-18-0055.1.xml.

Morrison, H., and Coauthors, 2020: Confronting the challenge of modeling cloud and precipitation microphysics. *Journal of advances in modeling earth systems*, **12 (8)**.

Pope, S. B., 2000: *Turbulent Flows*. Cambridge University Press.

Porté-Agel, F., M. Parlange, C. Meneveau, and W. Eichinger, 2001: A priori field study of the subgrid-scale heat fluxes and dissipation in the atmospheric surface layer. *Journal of the Atmospheric Sciences*, **58 (18)**, 2673–2698.

Prabhakaran, P., A. S. M. Shawon, G. Kinney, S. Thomas, W. Cantrell, and R. A. Shaw, 2020: The role of turbulent fluctuations in aerosol activation and cloud formation. *Proceedings of the National Academy of Sciences*, **117 (29)**, 16 831–16 838, https://doi.org/10.1073/pnas.2006426117, URL https://www.pnas.org/doi/abs/10.1073/pnas.2006426117.

Richter, D. H., T. MacMillan, and C. Wainwright, 2021: A Lagrangian cloud model for the study of marine fog. *Boundary-Layer Meteorology*, **181 (2)**, 523–542, https://doi.org/10.1007/s10546-020-00595-w, URL https://doi.org/10.1007/s10546-020-00595-w.

Salesky, S. T., K. Gillis, J. Anderson, I. Helman, W. Cantrell, and R. A. Shaw, 2024: Modeling the subgrid-scale scalar variance: A priori tests and application to supersaturation in cloud turbulence. *Journal of the Atmospheric Sciences*, **81 (5)**, 839 – 853, https://doi.org/10.1175/JAS-D-23-0163.1, URL https://journals.ametsoc.org/view/journals/atsc/81/5/JAS-D-23-0163.1.xml.

Shaw, R. A., 2003: Particle-turbulence interactions in atmospheric clouds. *Annual Review of Fluid Mechanics*, **35 (1)**, 183–227, https://doi.org/10.1146/annurev.fluid.35.101101.161125.

Shaw, R. A., W. C. Reade, L. R. Collins, and J. Verlinde, 1998: Preferential concentration of cloud droplets by turbulence: Effects on the early evolution of cumulus cloud droplet spectra. *Journal of the Atmospheric Sciences*, **55 (11)**, 1965 – 1976, https://doi.org/https://doi.org/10.1175/1520-0469(1998)055⟨1965:PCOCDB⟩

2.0.CO;2, URL https://journals.ametsoc.org/view/journals/atsc/55/11/1520-0469_1998_055_1965_pcocdb_2.0.co_2.xml.

Shawon, A. S. M., P. Prabhakaran, G. Kinney, R. A. Shaw, and W. Cantrell, 2021: Dependence of aerosol-droplet partitioning on turbulence in a laboratory cloud. *Journal of Geophysical Research: Atmospheres*, **126 (5)**, e2020JD033 799, https://doi.org/https://doi.org/10.1029/2020JD033799, URL https://agupubs.onlinelibrary.wiley.com/doi/abs/10.1029/2020JD033799.

Shima, S., K. Kusano, A. Kawano, T. Sugiyama, and S. Kawahara, 2009: The super-droplet method for the numerical simulation of clouds and precipitation: a particle-based and probabilistic microphysics model coupled with a non-hydrostatic model. *Quarterly Journal of the Royal Meteorological Society*, **135 (642)**, 1307–1320, https://doi.org/https://doi.org/10.1002/qj.441, URL https://rmets.onlinelibrary.wiley.com/doi/abs/10.1002/qj.441.

Stephens, G. L., and T. J. Greenwald, 1991: The earth's radiation budget and its relation to atmospheric hydrology: 2. observations of cloud effects. *Journal of Geophysical Research: Atmospheres*, **96 (D8)**, 15 325–15 340, https://doi.org/https://doi.org/10.1029/91JD00972, URL https://agupubs.onlinelibrary.wiley.com/doi/abs/10.1029/91JD00972, https://agupubs.onlinelibrary.wiley.com/doi/pdf/10.1029/91JD00972.

Stevens, B., and Coauthors, 2005: Evaluation of large-eddy simulations via observations of nocturnal marine stratocumulus. *Monthly Weather Review*, **133 (6)**, 1443 – 1462, https://doi.org/https://doi.org/10.1175/MWR2930.1, URL https://journals.ametsoc.org/view/journals/mwre/133/6/mwr2930.1.xml.

Sullivan, P. P., T. W. Horst, D. H. Lenschow, C.-H. Moeng, and J. C. Weil, 2003: Structure of subfilter-scale fluxes in the atmospheric surface layer with application to large-eddy simulation modelling. *Journal of Fluid Mechanics*, **482**, 101–139, https://doi.org/10.1017/S0022112003004099.

Thomas, L., W. W. Grabowski, and B. Kumar, 2020: Diffusional growth of cloud droplets in homogeneous isotropic turbulence: DNS, scaled-up DNS, and stochastic model. *Atmospheric Chemistry and Physics*, **20 (14)**, 9087–9100, https://doi.org/10.5194/acp-20-9087-2020, URL https://acp.copernicus.org/articles/20/9087/2020/.

Thomas, S., M. Ovchinnikov, F. Yang, D. van der Voort, W. Cantrell, S. K. Krueger, and R. A. Shaw, 2019: Scaling of an atmospheric model to simulate turbulence and cloud microphysics in the Pi chamber. *Journal of Advances in Modeling Earth Systems*, **11 (7)**, 1981–1994, https://doi.org/https://doi.org/10.1029/2019MS001670, URL https://agupubs.onlinelibrary.wiley.com/doi/abs/10.1029/2019MS001670.

Vaillancourt, P. A., and M. K. Yau, 2000: Review of particle-turbulence interactions and consequences for cloud physics. *Bulletin of the American Meteorological Society*, **81 (2)**, 285 – 298, https://doi.org/https://doi.org/10.1175/1520-0477(2000)081⟨0285:ROPIAC⟩2.3.CO;2, URL https://journals.ametsoc.org/view/journals/bams/81/2/1520-0477_2000_081_0285_ropiac_2_3_co_2.xml.

Vaillancourt, P. A., M. K. Yau, P. Bartello, and W. W. Grabowski, 2002: Microscopic approach to cloud droplet growth by condensation. part ii: Turbulence, clustering, and condensational growth. *Journal of the Atmospheric Sciences*, **59 (24)**, 3421 – 3435, https://doi.org/https://doi.org/10.1175/1520-0469(2002)059⟨3421:MATCDG⟩2.0.CO;2, URL https://journals.ametsoc.org/view/journals/atsc/59/24/1520-0469_2002_059_3421_matcdg_2.0.co_2.xml.

Yau, M., and R. Rogers, 1996: *A Short Course in Cloud Physics*. Elsevier Science, URL https://books.google.com/books?id=ClKbCgAAQBAJ.